Recent Milestones in Unraveling the Full-Field Structure of Dynamic Shear Cracks and Fault Ruptures in Real-Time: From Photoelasticity to Ultrahigh-Speed Digital Image Correlation

A. J. Rosakis[1]
Graduate Aerospace Laboratories,
California Institute of Technology,
Pasadena, CA
e-mail: arosakis@caltech.edu

V. Rubino
Graduate Aerospace Laboratories,
California Institute of Technology,
Pasadena, CA
e-mail: vito.rubino@caltech.edu

N. Lapusta
Mechanical and Civil Engineering,
Seismological Laboratory,
California Institute of Technology,
Pasadena, CA
e-mail: lapusta@caltech.edu

The last few decades have seen great achievements in dynamic fracture mechanics. Yet, it was not possible to experimentally quantify the full-field behavior of dynamic fractures, until very recently. Here, we review our recent work on the full-field quantification of the temporal evolution of dynamic shear ruptures. Our newly developed approach based on digital image correlation combined with ultrahigh-speed photography has revolutionized the capabilities of measuring highly transient phenomena and enabled addressing key questions of rupture dynamics. Recent milestones include the visualization of the complete displacement, particle velocity, strain, stress and strain rate fields near growing ruptures, capturing the evolution of dynamic friction during individual rupture growth, and the detailed study of rupture speed limits. For example, dynamic friction has been the biggest unknown controlling how frictional ruptures develop but it has been impossible, until now, to measure dynamic friction during spontaneous rupture propagation and to understand its dependence on other quantities. Our recent measurements allow, by simultaneously tracking tractions and sliding speeds on the rupturing interface, to disentangle its complex dependence on the slip, slip velocity, and on their history. In another application, we have uncovered new phenomena that could not be detected with previous methods, such as the formation of pressure shock fronts associated with "supersonic" propagation of shear ruptures in viscoelastic materials where the wave speeds are shown to depend strongly on the strain rate. [DOI: 10.1115/1.4045715]

Keywords: earthquake source physics, rupture dynamics, dynamic friction, supershear and supersonic ruptures, digital image correlation

1 Introduction

Dynamic shear ruptures propagating along incoherent (or frictional) interfaces are relevant to a wide range of applications from engineering [1,2] to geophysics [3–6], including composite delamination and earthquake ruptures propagating along faults in the Earth's crust. Friction and its evolution determine how these ruptures propagate and arrest, ultimately affecting failure and damage [7,8]. Yet friction during dynamic ruptures has been the subject of vigorous debate and capturing its evolution has been one of the greatest challenges in experimental mechanics. Full-field visualization of dynamic ruptures has been confined for decades to optical techniques such as coherent gradient sensing (CGS) and photoelasticity providing only limited field information near the rupture tip. In particular, CGS provides gradients of out-of-plane displacements when used in reflection and gradients of direct stress when used in transmission, while photoelasticity furnishes maximum shear stress fields, being insensitive to dilatational information. While none of these techniques is capable of providing individual displacement, strain, and stress components, they have been invaluable in enabling our first important steps in the experimental discovery of "intersonic" or "supershear" ruptures in a wide variety of bimaterial, composite, and frictional systems of relevance to both Engineering and Geophysics [9] and for the creation of the "laboratory earthquake" concept for studying model earthquakes under controlled conditions in the laboratory [10].

We start this paper by briefly summarizing some milestones achieved in our laboratory over the last 30 years using previous technology including photoelasticity and CGS. We then review our recent progress in the study of dynamic ruptures enabled by the leap from previous diagnostics to ultrahigh-speed digital image correlation (DIC). The new diagnostics has allowed us to visualize and quantify dynamic ruptures at a level of detail that until recently was only available with numerical simulations. We then describe some of the main advances enabled by the new approach, including (1) tracking the evolution of dynamic friction which has given us the possibility of testing proposed friction formulations; (2) imaging the variation of mechanical fields of dynamic ruptures, which has allowed us to quantify ground shaking signatures near rupturing faults and to discover new phenomena, such as the formation of pressure shock fronts associated with the propagation of "supersonic" shear ruptures in viscoelastic materials; (3) pushing beyond our current capabilities to estimate the out-of-plane displacement and velocity fields near the growing ruptures with an outlook towards future 3D measurements.

---

[1]Corresponding author.

2 Milestones in the Characterization of Dynamic Ruptures in Our Laboratory Using Photoelasticity and Coherent Gradient Sensing

Shear cracks are usually not observed experimentally in homogeneous and isotropic solids, since cracks subjected to mode II or mixed loading typically curve or kink in order to propagate in a direction with locally mode I conditions at the crack tip [11–13]. There are three conditions that promote mode II crack propagation: a high confining stress level preventing crack opening [14,15], a specifically designed specimen geometry [16,17], and the presence of a weak layer determining the crack path. Indeed, dynamic mode II cracks have been observed experimentally in inhomogeneous solids containing a weak layer, typically a glued bond with a lower fracture toughness [9]. One question that has attracted researchers for decades is that of crack speed in relation to radiated energy, due to its importance across many disciplines [1,5,9,10,18–22]. Due to energy considerations and singular elastodynamics, mode II cracks propagating in linear elastic isotropic solids have two permissible crack speed regimes: below the Raleigh wave speed c_R (so-called sub-Rayleigh cracks) or between the shear c_s and longitudinal c_p wave speeds [1,9,23]. Cracks in the latter regime are referred to as "intersonic" or "supershear." The speed regime between the Rayleigh and the shear wave speed is forbidden based on energy considerations. As a consequence, according to singular elastodynamics, shear cracks could be either sub-Rayleigh or purely intersonic and could not transition between the two regimes with a continuous variation of crack speed [1]. However,

no experimental evidence of intersonic crack growth was available at that time.

In bimaterial systems involving different elastic properties across the interface, there are two sets of wave speeds associated with different elastic properties. When there is a sufficiently high mismatch in the wave speeds of the two constituents, theoretical studies showed that a shear crack propagating at sub-Rayleigh speed with respect to the stiffer solid may propagate at intersonic speed with respect to the wave speeds of the more compliant solid [24]. The first experiments aimed at the observation of intersonic shear crack growth were conducted in bi-materials bonded along a weak interface [25–28] and were indeed able to provide the first experimental proof of intersonic rupture in such systems. An example of intersonic rupture along the bimaterial Homalite/steel interface is reported in Fig. 1(a) [29]. The isochromatic fringe patterns, produced by photoelasticity, reveal the formation of multiple Mach fronts, revealing the intersonic nature of the crack. Note that the formation of multiple fronts is due to the finite contact zone behind the crack tip in a bimaterial interface [29–31].

Intersonic cracks in a constitutive homogeneous, linear elastic system involving weakly bonded identical solids were not thought to be possible. The experimental discovery [32] of the elusive intersonic cracks growing along the weak interface in a constitutively homogeneous solid, with only one set of wave speeds, demonstrated that this was not the case. It was shown that, as the crack propagated under sufficiently high shear loading, provided by asymmetric impact loading, it developed a distinct "Shear Mach Cone," the existence of which provided conclusive proof of
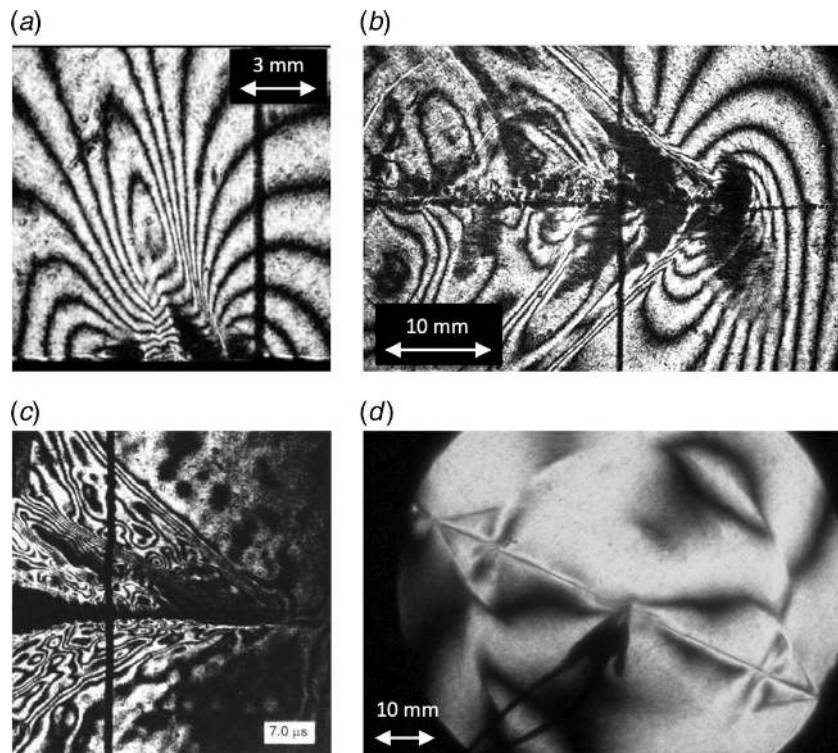
Fig. 1 Fringe patterns showing the formation of shock fronts associated with the propagation of intersonic or supershear cracks, produced using photoelasticity or coherent gradient sensing (CGS) techniques. (a) Photoelastic isochromatic fringe pattern displaying a crack propagating along the bimaterial Homalite/steel interface at a speed of 1.15c_s [29] with the formation of multiple Mach fronts. (c) Photoelastic images showing unilateral crack propagating along the coherent interface separating two weakly bonded plates of Homalite [32], (b) CGS interferograms showing shear crack propagation along the fibers of a unidirectional graphite-epoxy composite laminate at a speed in excess of 7.5 km/s [33]; (d) Photoelastic images showing bi-lateral rupture propagating along a purely frictional (incoherent) interface in Homalite displaying two symmetric Mach cones associated with supershear rupture propagation [21].

the existence of intersonic cracks in nature (Fig. 1(*b*)). Another dramatic example of intersonic propagation is the shear crack growing parallel to the fibers of a unidirectional graphite-epoxy composite laminate [33,34]. The propagating crack again develops visible shock fronts (Fig. 1(*c*)), showing that it has exceeded the shear wave speed along the fiber direction. The rupture presented in Fig. 1(*b*) actually propagates at speeds in excess of 7.5 km/s which is comparable to the P-wave speeds in the fiber direction of the anisotropic, but homogenized graphite fiber/epoxy matrix system, and is the fastest cracks recorded to date. In that experiment, the technique of CGS by reflection, which is sensitive to the gradients of the out-of-plane displacements along the direction parallel to the interface, is used to visualize the shock waves associated with this nearly "sonic" shear rupture in this opaque solid.

The discovery of supershear ruptures in constitutively homogeneous systems with weak interfaces, created a strong resonance with the geophysics community where dynamic rupture propagation is at the heart of seismology because of its role in creating earthquakes and its importance in the study of earthquake hazard mitigation. Supershear propagation of earthquakes had been suspected by a number of early seismic inversion studies, e.g., Refs. [35–37], but one conceptual difficulty in widely accepting these studies, in addition to the non-unique nature of the inversion problem, was how an earthquake rupture could possibly overcome the energy barrier found at the Rayleigh wave speed and thus transition to supershear speed [9].

One theoretical mechanism for the sub-Rayleigh to supershear transition that had been proposed many years before was the Burridge-Andrews transition mechanism [38,39]. According to this mechanism, a rupture propagating at a sub-Rayleigh speed features a growing peak in shear stress ahead of the rupture tip. The shear stress peak travels at the shear wave speed, above the energy barrier. When the peak in stress reaches shear strength, a secondary rupture is nucleated ahead of the main one and travels at supershear speeds. Despite these theoretical studies, the seismological community remained largely unconvinced that frictional interfaces, such as geological faults, could host supershear ruptures. Indeed, and until 1999, there was no experimental evidence that interfacial ruptures in homogeneous systems could either be born supershear or ever transition to such high speeds. Furthermore, there were no laboratory evidence that these phenomena could ever happen in frictional (rather than in coherent) interfaces and under conditions of static tectonic loading mimicking the conditions in the earth's crust. This proof was not furnished until the early 2000s when Xia et al. [21] created the first "Laboratory Earthquake" setup. Through this setup, which involved frictionally held plates subjected to compression and shear, mimicking frictional faults under tectonic loading conditions, they were able to again observe the occurrence of "spontaneous" rupture propagation at supershear speeds. Furthermore, they provided the first experimental observation of sub-Rayleigh to supershear transition in the laboratory that confirmed beyond doubt the possibility of this phenomenon [21]. One important advancement of this setup versus previous experimental configurations featuring impact loading, e.g., Refs. [32,40] is that, while the nucleation is controlled, once nucleated, ruptures propagate spontaneously [10]. An example of bi-lateral rupture propagation featuring the formation of two Mach cones is shown in Fig. 1(*d*). The experimental discovery of supershear transition has motivated seismologist to look closer at field evidence for earthquakes propagating at supershear speed, and as a result, the reporting of such events, formerly thought to be rare, have significantly multiplied [41–45]. Observations of supershear ruptures were also paralleled by numerous experimental and numerical studies [46–55].

Since year 2000, the "Laboratory Earthquake" concept and setup [10,21] has been extensively used to study a number of fundamental rupture dynamics phenomena, including rupture directionality in bimaterial and damaged media [56–58], pulse-like to crack-like transition with changing pre-stress [59,60], dynamic off-fault damage creation [61], properties of sub-Rayleigh and supershear

ruptures and attenuation [62,63], and rupture interaction with the free surface [64,65]. The diagnostics used in these early "Laboratory Earthquake" studies was based on either dynamic photoelasticity, which provides the full-field maximum shear stress in a semi-quantitative fashion (using the stress optic law) with temporally sparse acquisition or temporally active but spatially sparse laser velocimeters, which were available only at two to three locations per test [10]. One limitation of the diagnostics used in earlier studies is that it could not quantify the full-field temporal evolution of displacements, velocities, strains or stress components. This called for a shift in paradigm in the laboratory measurements.

3 From Photoelasticity to Digital Image Correlation

The advent of DIC has transformed the field of experimental mechanics with multifold new applications [66–68]. Digital image correlation is a versatile optical technique that compares images of the deformed and reference/undeformed configurations to determine the displacement fields, which can then be used to compute derived quantities such as velocities and strains [66]. The correlation can be performed using either a local or a global approach [69,70]. In the local methods, image matching is performed over small windows referred to as "subsets" separated by a distance known as the "step" size [66,71,72]. In the global approaches, the correlation is performed accounting for the entire domain, typically using finite element formulations [73,74].

In the new phase of evolution of our "Laboratory Earthquake" setup, we have recently been able to quantify the full-filed behavior of dynamic ruptures using digital image correlation combined with ultrahigh-speed photography [75–78]. The setup (Fig. 2) comprises a specimen loaded in compression and shear (similar to earlier versions of this setup, e.g., Ref. [10]) made of a brittle polymer (typically Homalite-100), an ultrahigh-speed camera (with a frame rate up to 10 million frames/s), a white light source (capable of providing enough illumination for the short exposures used), and a high-voltage capacitor (providing a controlled rupture initiation through a small wire burst). The specimen is characterized by an interface inclined at an angle α (Fig. 2). The uniaxial compressive load P results in resolved shear stress $\tau_0 = P \sin \alpha \cos \alpha$ and normal stress $\sigma_0 = P \cos^2 \alpha$. One important property of the ruptures produced in this setup is that, once initiated, they propagate spontaneously driven by the level of applied pre-stress (similarly to Ref. [21]). The high-speed camera has a resolution of 400×250 pixels^2 and is equipped with a number of different prime lenses, in order to focus on fields of view of different sizes, ranging from 145×91 mm^2 to 5.6×3.5 mm^2. The inset of Fig. 2 shows the position and orientation of two fields of view that we discuss in this work.

3.1 Static Measurements of Dynamic Ruptures Using Digital Image Correlation. As a first step toward the implementation of digital image correlation to capture dynamic ruptures, we started quantifying the static fields associated with arrested dynamic ruptures (Fig. 3; Ref. [79]). While using DIC in these laboratory measurements offers a unique opportunity to study rupture features in its own right, one motivation for this work was to investigate the feasibility of real-time full-field earthquake measurements from space, enabled by the development of the space optical seismometer [79,80]. This new concept would be based on a geostationary satellite featuring an optical telescope capable of a high-density spatiotemporal sampling. The telescope would be acquiring digital images in real-time during earthquake propagation. Concurrently, the laboratory-based static measurements can also help interpret current air- and space-borne measurements, obtained by taking images before and after earthquakes, whose interpretation is not straightforward due to the inherent complexity of natural faults and deformation fields. In our experiments, the lateral portions of the specimens were glued in order to confine the rupture in the central portion of the interface.
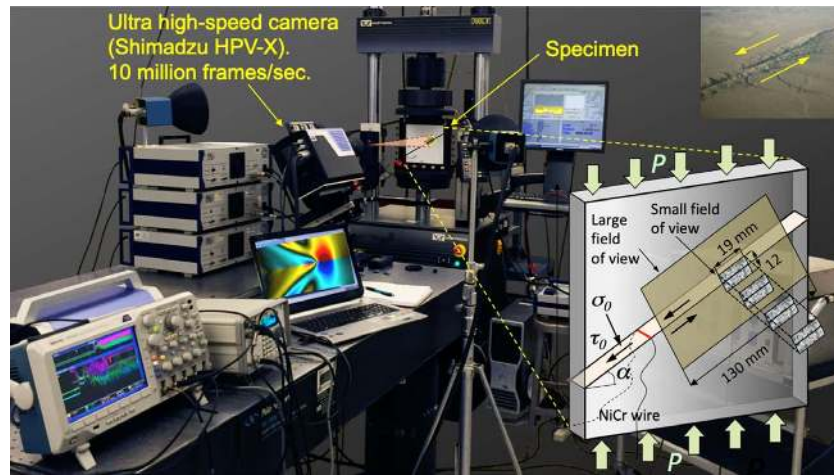
Fig. 2 The second-generation "laboratory earthquake" setup at Caltech employed to study dynamic rupture propagation with ultrahigh-speed digital image correlation (DIC) and laser velocimeters. Earthquakes are mimicked in the laboratory by dynamic rupture propagation along the frictional interface of two Homalite plates pre-loaded in compression and shear. An ultrahigh-speed camera captures a sequence of deformed images that are analyzed with pattern matching algorithms to produce full-field maps of displacements, velocities, and strains. Velocimeters are simultaneously employed either to compare with the DIC time histories or to have measurements outside the field of view imaged with DIC. Top right inset shows an image of the strike-slip the San Andreas fault[2] (copyright David K. Lynch). Bottom right inset shows a specimen configuration with two typical fields of view.
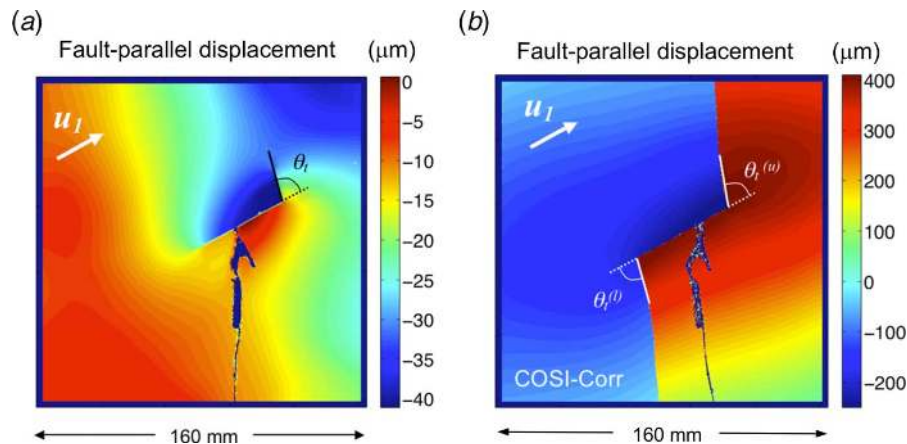
Fig. 3 Fault-parallel displacement maps of two dynamic ruptures arrested at the glued boundaries of the specimen. (a) Sub-Rayleigh and (b) supershear rupture produced with $P = 5$ MPa and $P = 15$ MPa, respectively. Both specimens have a fault inclination angle of $\alpha = 29$ deg. The specimens have glued regions at the lateral portions of the interface in order to confine the propagating dynamic rupture to a finite length and to capture the displacement field associated with the arrested rupture. In both cases, rupture attests result in the formation of wing cracks, which are more pronounced in the case of higher load.

Images of the specimen taken with a high-resolution and low-frame-rate camera before and after rupture propagation allow capturing the static field of the arrested cracks. As the rupture encountered the glued edges, it was arrested abruptly forming secondary cracks (Fig. 3). The resulting wing cracks were more pronounced for higher pre-load cases. The formation of wing cracks is an interesting phenomenon that has been found in a wide range of earth and planetary science phenomena. For example, secondary cracks have been observed on opposite ends of a fault, as a result of the faulting process [81–86], associated with splitting, exfoliation, and rock burst [12], and have also been observed at the tip of strike-

slip faults in the ice shell of Europa, Jupiter's moon [87]. While these initial static measurements allowed interesting observations, they did not allow to capture the evolution of dynamic ruptures.

3.2 Challenges in Developing Ultrahigh-Speed Digital Image Correlation to Capture Dynamic Ruptures. The digital image correlation method has been successfully applied in a variety of dynamic applications [88–94]. However, quantifying with DIC the full-field evolution of dynamic ruptures traveling at speeds in the range of several kilometers per second (typically 1 km/s for a sub-Rayleigh rupture and up to about 2.6 km/s for a supershear rupture) has its own set of challenges, requiring a temporal acquisition on the order of 1–2 MHz, in order to capture the

rapid temporal variations associated with highly transient phenomena, as well as an adequate spatial sampling to describe the spatial gradients associated with the presence of shock fronts and other sharp features. In addition, when processing digital images with DIC algorithms, the noise level of the camera needs to be extremely low, as it affects the quality of the displacement fields and especially the fields obtained through temporal and spatial differentiation, such as velocities and strains. These are very stringent requirements for a high-speed camera, since cameras in the ultrahigh-speed range (0.5 million frames/s and above) were traditionally based either on gate-intensified technology (which produces noisy images) or rotating mirror systems (which can produce operational challenges at high-frame rates due to the elevated rotating speeds) [77,95–97]. On the other hand, cameras that have low noise levels typically are in the low range of frame rates, below what is needed for highly dynamic ruptures [77,96,97]. In addition, the high-speed systems acquire images via the presence of multiple sensors, which can introduce further complications in the process of correlation [77]. An alternative camera technology, based on image acquisition and recording on an individual sensor and with lower noise levels, started being developed in the early 2010s [98,99]. In our first attempts to capture dynamic rupture propagation, we used early versions of this camera technology (i.e., the Shimadzu HPV-2), which allowed us to quantify the displacement field of supershear ruptures [100]. However, the noise level of these measurements was not low enough to accurately compute strains and stresses and to describe other important quantities, such as the evolution of dynamic friction. A technology complying with all the specifications mentioned above did not become available in the market until the mid-2010s (Shimadzu HPV-X), when we were finally able to measure velocities, strains, and stresses of supershear ruptures [101].

3.3 Full-Field Measurements of the Evolution of Dynamic Ruptures.
These advances enabled the leap from photoelasticity to digital image correlation (Fig. 4; Ref. [77]). Images of the deformed specimens are typically acquired at 1–2 million frames/s. The field of view is marked with a random speckle pattern in order to provide a characteristic texture for image correlation. The acquired images are processed with (local) DIC algorithms to produce evolving maps of displacements. Correlations are typically performed with a subset size of 41×41 pixels^2 and a step size of 1 pixel [77]. Displacements are then filtered using a non-local means filter [79,102–104]. Particle velocity fields are determined by applying a central difference scheme in time. Strain changes are computed with a central difference scheme in space, and stress changes are obtained assuming linear elasticity and by using a dynamic Young's modulus. The total levels of stress are obtained by adding the resolved level of applied pre-stress [77].

Another challenge involved in the measurements of shear ruptures with DIC is that most image matching algorithms are developed assuming a continuous displacement field. These approaches cannot be used to quantify shear cracks, which are characterized by a displacement jump across the interface. Other DIC approaches have been developed to analyze discontinuous fields [105–111], but they are based on theoretical assumptions, which limit the range of applicability of these methods. In our studies, we employ a commercial software package (VIC-2D; Correlated Solutions Inc.) enhanced to treat interfaces with displacement discontinuities [77]. In this approach, image correlation is performed based on local methods; the displacements are computed up to half a subset away from the interface and are extrapolated to the interface using affine transformation functions. The fields obtained using this approach may suffer from slight deviations from symmetry for quantities that are supposed to be symmetric. Another limitation is that the stresses computed from the displacements and strain fields may not satisfy traction continuity conditions. In order to tackle these issues and reduce the effects of measurement errors, we have developed a methodology to enforce traction continuity along the interface [78] and symmetry/anti-symmetry of the analyzed fields [77].

Using the new ultrahigh-speed DIC diagnostics, we are able to see beyond the limited information provided by previous diagnostics and can continuously map quantities that were not possible to measure before, including the displacement and strain components. An example of displacement and strain fields for a rupture captured with the small field of view shown in Fig. 2 (19×12 mm^2) is reported in Fig. 5. Note that the processed fields are slightly cropped compared with the imaged field of view. The fault-parallel displacement clearly shows the shear motion experienced by the fault (Fig. 5(*a*)). More interestingly, the full-field maps of the fault-normal displacement reveal that the fault has an upward motion in a small region near the rupture tip, followed by a motion in the opposite direction involving not only the near-tip region but also the far-field (Fig. 5(*b*)). The shear strain (Fig. 5(*c*)) is used to compute the shear stress, and it is the key to compute the evolution of dynamic friction, as explained in Sec. 5.

4 Advancement Over Previous Velocimeter Measurements

We have verified the accuracy of DIC measurements by comparing the velocity-time histories produced by DIC to independent
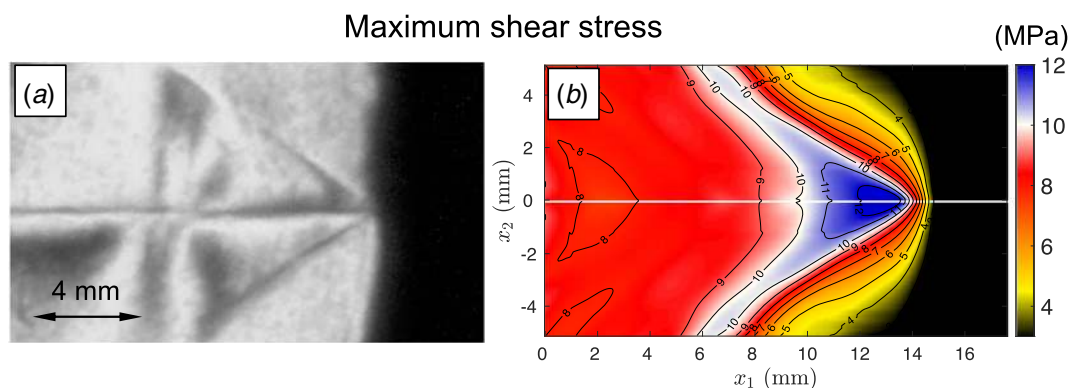
Fig. 4 Comparison of the Mach cone displayed by supershear ruptures imaged by photoelasticity and ultrahigh-speed digital image correlation (DIC) measurements (modified after Ref. [77]). (*a*) Isochromatic fringe pattern obtained with photoelasticity [21] associated with the maximum shear stress, (*b*) full-field map of the maximum shear stress with overlaid contour plot, obtained using DIC. The dynamic DIC measurements not only allow visualization of key rupture features, as it was the case with previous techniques such as photoelasticity or CGS, but also allow direct quantification of the dynamic rupture behavior by tracking the full-field evolution of a range of other quantities not accessible by other techniques.
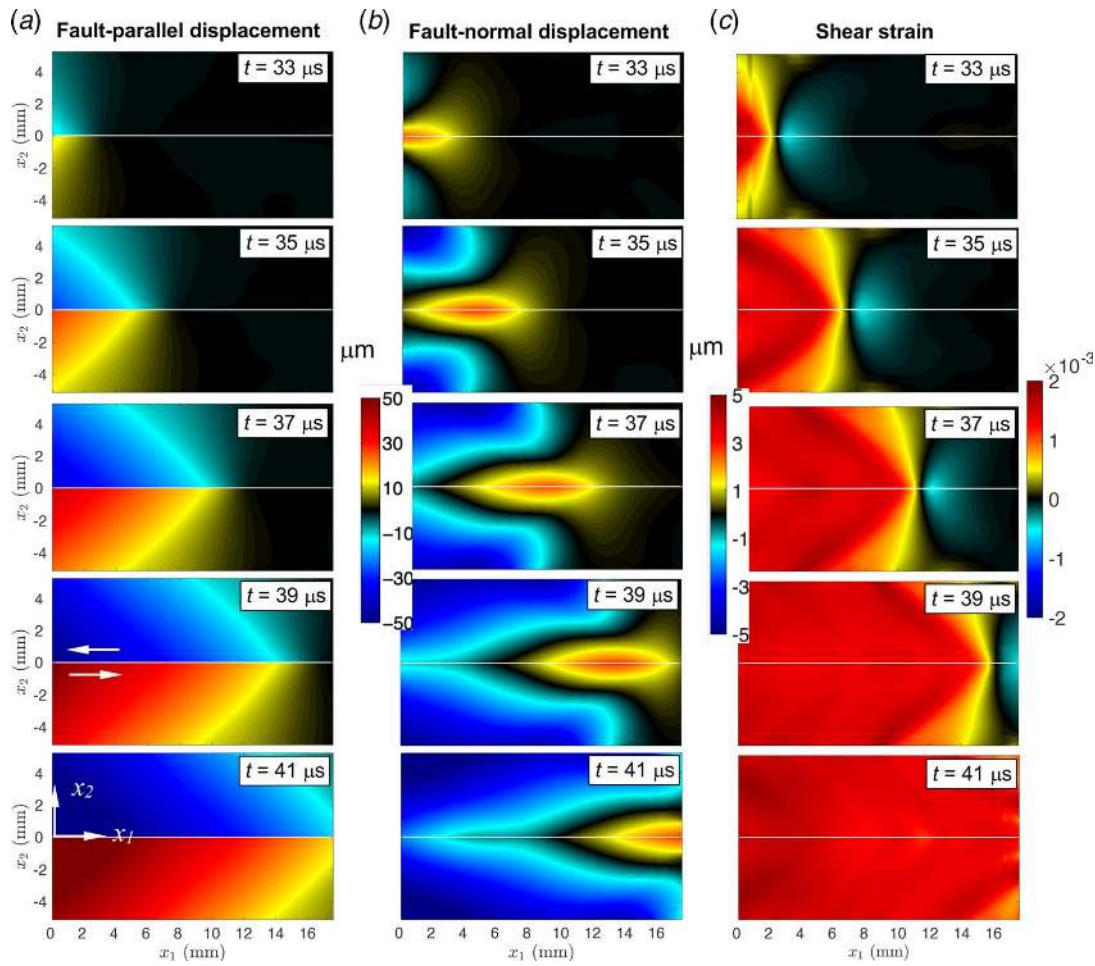
Fig. 5 Full-field sequence of the displacements and strains associated with a supershear rupture, produced under a compressive pre-stress of $P = 23$ MPa, and a fault inclination angle $\alpha = 29$ deg. (a) Fault-parallel and (b) fault-normal displacements; (c) shear strain change using the pre-loaded state as reference configuration. The rupture presented here is the same reported in Refs. [75,77]. While the fault-parallel displacement maps highlight the shear motion, the fault-normal displacement maps show that the fault line itself does not remain straight during rupture propagation but that it rather undulates up and down. The shear strain illustrates an initial small change at the rupture tip followed by a more pronounced variation.

measurements obtained with the well-developed techniques of laser velocimetry [62,112] at the same locations and during the same experiments. The position of velocimeter measurements is shown in Fig. 6(a), together with the size of the field of view selected for this comparison (50×31 mm^2). Note that fields of view much smaller than the one indicated in Fig. 6(a) cannot be used for the comparison, as the size of the reflective tape becomes too large when compared with the subset size used for the correlation. The comparison of Fig. 6(b) shows excellent agreement between the two sets of measurements [75]. The velocity-time histories obtained with DIC are also in agreement with laser velocimeter measurements obtained at various locations in numerous other experiments reported in previous studies [62,63]. These comparisons give confidence that the DIC measurements can accurately describe the velocities time histories at any point within the field of view with a spatial resolution of 400×250 pixels^2, corresponding to having virtually 100,000 velocimeters. This is a major development since previous velocimeter measurements, only available at two to three locations per test, required a large number of tests to have a still sparse coverage of the velocity structure.

We can use the temporal evolution of the particle velocity maps to visualize their spatiotemporal structure (Figs. 6(c) and 6(d)) and study key rupture features (see Secs. 5–7). The dense spatial resolution together with high-frequency temporal sampling allows reconstructing with high fidelity the combined spatiotemporal

behavior of dynamic ruptures (Fig. 6(e)). One note of caution is that while laser velocimeters are point-wise measurements, DIC involves spatial averaging through subsets, in order to regularize the non-uniqueness of the pixel-by-pixel correlation problem. The spatial smoothing increases with larger subset sizes. As the field of view increases, so does the subset size, in order to maintain the same level of noise as smaller fields of view. When the physical size of the subset becomes comparable or larger than characteristic length-scales of the rupture, these features are filtered out. At the same time, if the physical size of the subset is maintained constant with increasing size of the field of view, the displacement fields become too noisy to produce velocity, strain or strain rate fields. For example, the velocity profile traced along the interface with an intermediate-sized field of view (50×31 mm^2) and a subset size of 41×41 pixels^2 shows the presence of two peaks (light green line in Fig. 6(c)), reflecting the time history of Fig. 6(b). Conversely, the velocity profile obtained with a larger field of view (131×81 mm^2) and a subset of the same size (41×41 pixels^2) filters out the double peak feature (light green line in Fig. 6(d)), since the physical size of the subset increases with the field of view. Yet, the particle velocity map of Fig. 6(d) has important information that would not be possible to interpret from maps with higher noise level resulting from using smaller subset sizes. Hence, a compromise is to use small fields of view to capture fine details and large imaging windows
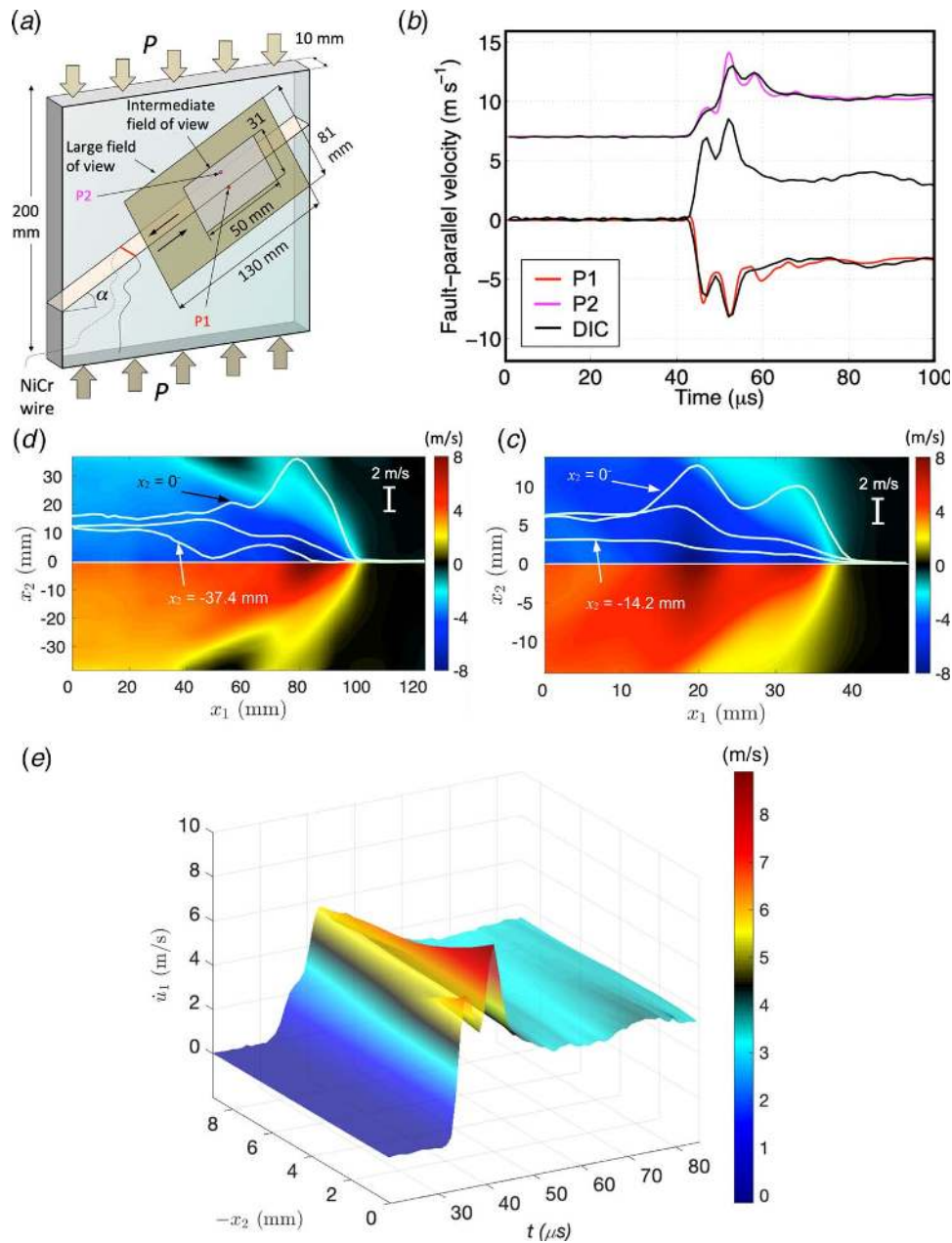
Fig. 6 Comparison between digital image correlation (DIC) and velocimeter measurements.
(a) Schematic of the specimen configuration showing the size of the field of view used for DIC as well as the location of the velocimeter measurements; (b) particle velocity time history obtained from the velocimeters and extracted at corresponding locations from the full-field DIC measurements [75]; (c) full-field velocity map from which the time histories of (b) are extracted with overlaid selected curves of particle velocity versus x_1 at different values of x_2; (d) full-field velocity map obtained from DIC [77] with overlaid particle velocity curves along lines parallel to the interface; (e) particle velocity time histories plotted along the (negative) x_2-axis, for a point at the center of the field of view of the measurements in (c). While previous velocimeter measurements could only achieve a sparse coverage at two to three locations, the DIC-based measurements can achieve a nearly continuous mapping of the velocity field with comparable accuracy.

to study the far-field structures [77]. The next two sections show how to quantify key rupture phenomena by appropriately selecting the size of the field of view.

5 Capturing the Evolution of Dynamic Friction

The way dynamic ruptures propagate along faults in the Earth's crust and release waves that cause destructive shaking is controlled by the evolution of friction [8,113]. Assumptions about dynamic friction affect a wide range of earthquake science studies, including energy partitioning, rupture modes, stress levels on faults, and patterns of seismic/aseismic slip [59,114–122]. Yet how dynamic friction evolves during earthquake ruptures remains one of the key questions in earthquake science [8]. As an earthquake rupture propagates, the two sides of a fault slide past each other, accumulating relative displacement, or slip, with average slip rates on the order of 1 m/s. One point to address regarding dynamic friction is whether its evolution is controlled by slip or slip rate. In a recent study [75], we have reported local measurements of evolving friction,

during spontaneously propagating dynamic ruptures, using the setup shown in Fig. 2. One advantage of our approach is that we have the dynamic recording capability to follow individual ruptures and to study the evolution of friction as these ruptures pass by at very high speeds. We thus do not have to assume that interfaces slide uniformly as is done in traditional methods of studying friction. Another advantage is that our laboratory setup (Fig. 2) allows us to produce dynamic ruptures with markedly different slip and slip rate histories, resulting in significantly different friction behavior.

Let us consider a rupture produced with an applied vertical load of $P = 23$ MPa and $\alpha = 29$ deg (Fig. 7). As the rupture arrives, the fault-parallel velocity field shows the particle velocity rapidly increasing, with opposite sign on each side of the interface, up to an absolute value ~ 10 m/s and then decreases to a lower steady-state level revealing the crack-like nature of this rupture (Figs. 7(a) and 7(c)). The shear stress increases up to a peak of $\tau_p \sim 11.8$ MPa from the uniform pre-stress level of $\tau_0 = P \sin \alpha \cos \alpha = 9.8$ MPa before rupture arrival (Figs. 7(b) and 7(d)). Behind the rupture tip, the shear stress decreases to a dynamic level of $\tau_d \sim 4.6$ MPa. Using the fault-parallel displacement and velocity maps, we determine the slip and slip rate, respectively, by computing the difference between pixels just above and below the interface. Friction is obtained by the ratio of the shear to normal stress along the interface. Let us now consider another rupture, produced with an applied vertical load of $P = 7.4$ MPa and $\alpha = 29$ deg. Tracking the particle velocity and shear stress along the interface (Figs. 7(c) and 7(d), respectively) reveals that the behavior in this case is qualitatively similar to the previous test but with lower levels of particle velocities (with a peak level of ~ 2 m/s) and shear stress (peak of $\tau_p \sim 11.8$ MPa).

The dependence of friction on the slip and slip rate for these two cases is reported in Figs. 8(a) and 8(b), respectively. The friction versus slip curves show that, in both cases, friction initially rapidly increases and then gradually drops to a residual level, which remains nearly constant with increasing levels of slip (Fig. 8(a)). This behavior qualitatively resembles that described by a linear slip-weakening friction law, where the friction coefficient f evolves with slip δ according to

$$
f = \begin{cases} f_s - (f_s - f_d)\dfrac{\delta}{D_c}, & \delta \leq D_c \\ f_d, & \delta > D_c \end{cases} \tag{1}
$$

where f_s and f_d are the static and dynamic friction coefficients, and D_c is the slip distance over which f_d is reached. In the linear slip-weakening friction law, the parameters f_d and D_c are material properties. However, the two ruptures of Fig. 8(a) result in different values of f_d and D_c, indicating that a unique slip-dependent law cannot describe the friction evolution of the interface and that the parameters f_d and D_c are effective quantities and not material properties characteristic of the interface.

The friction versus slip rate curves display a dramatically different response for the two ruptures. They indicate that the friction evolution cannot be captured by a purely rate-dependent friction law either. The two curves exhibit some common features, including initial strengthening with slip rate, subsequent weakening, and attainment of steady-state for nearly constant slip rate. The rupture produced with a higher pre-load ($P = 23$ MPa) reaches a dynamic level of $f_d = 0.26$ for a steady-state slip rate level of $V_{ss} = 6.5$ m/s, while the rupture produced with lower pre-stress ($P = 7.4$ MPa) attains $f_d = 0.39$ at $V_{ss} = 0.87$ m/s (Fig. 8). These observations are consistent with the rate-and-state friction formulation, where friction is a function of the slip rate $\dot\delta = V$ and of a state variable θ describing the evolution of the contacting asperities [123–129]:

$$
f = f_* + a \log\left(\frac{V}{V_*}\right) + b \log\left(\frac{V_* \theta}{L}\right) \tag{2}
$$
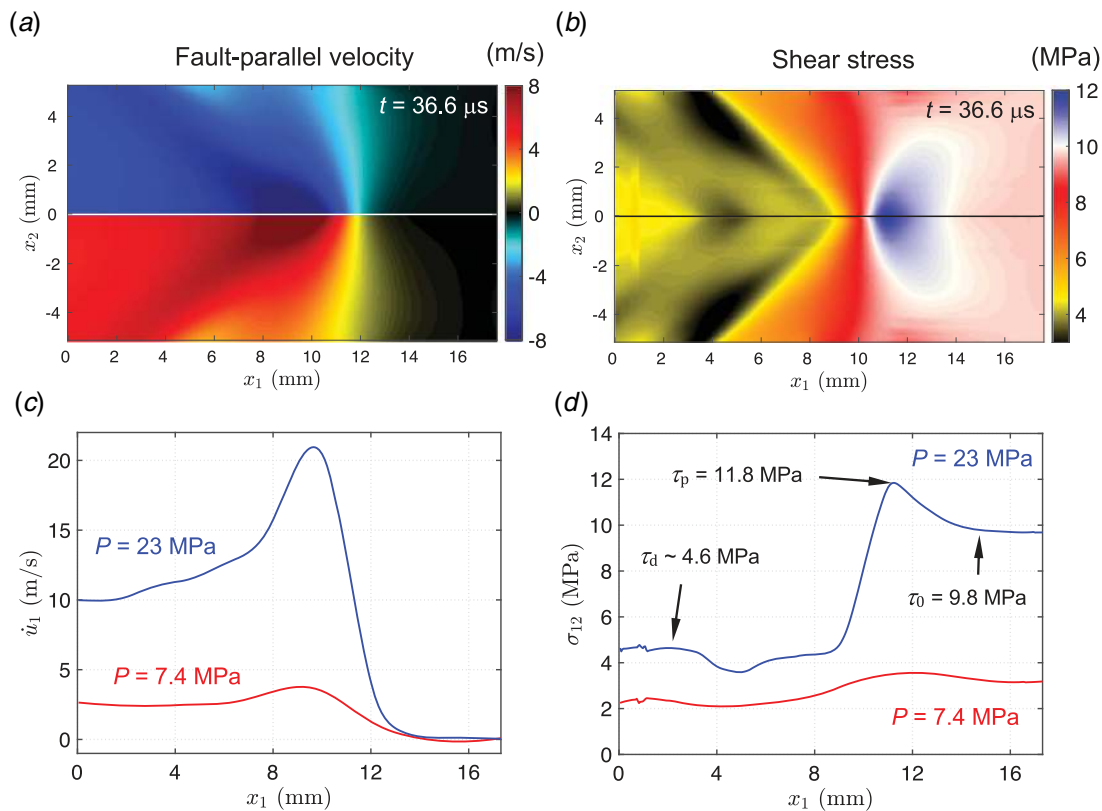
Fig. 7 Particle velocity and shear stress for two supershear ruptures under different experimental conditions. (a) Fault-parallel velocity and (b) shear stress fields for the supershear rupture of Fig. 4 ($P = 23$ MPa and $\alpha = 29$ deg), from Refs. [75,77]. (c) On-fault particle velocity and (d) shear stress versus position for two supershear ruptures, obtained with a pre-stress of $P = 23$ MPa and $P = 7.4$ MPa (blue and red curves, respectively), both with $\alpha = 29$ deg.
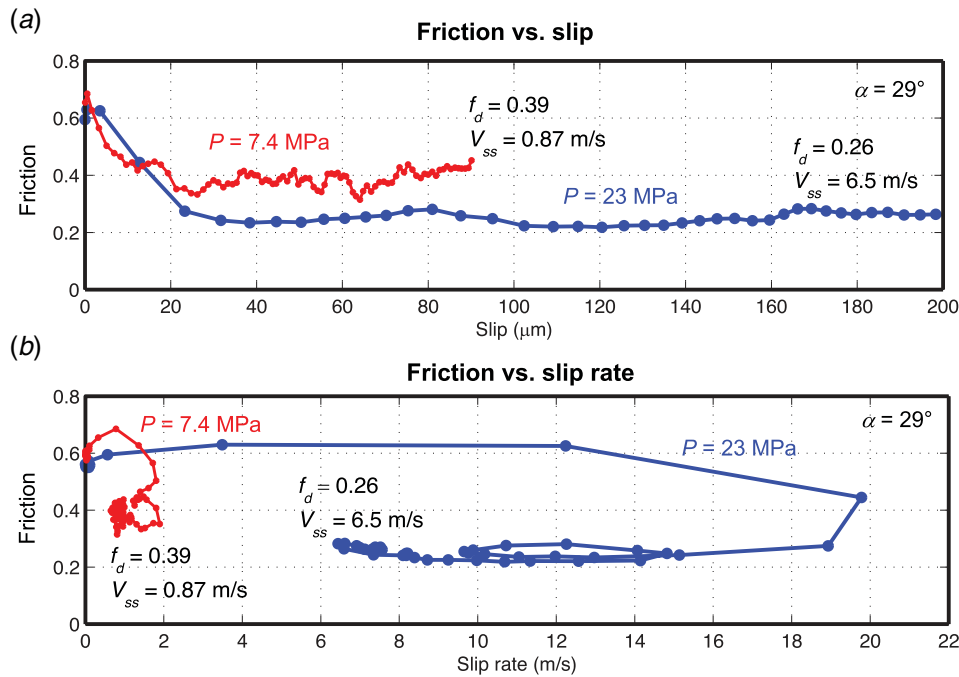
Fig. 8 Evolution of dynamic friction obtained from measurements performed during the spontaneous propagation of two individual dynamic ruptures (modified from Ref. [75]). (*a*) Friction versus slip and (*b*) friction versus slip rate. Friction weakens with slip, qualitatively resembling some slip-weakening friction laws. However, the intensity of weakening, i.e., the coefficient of dynamic friction, is not a function of slip only. Indeed, the evolution of friction with slip rate shows a complex relation, revealing a strong but complex dependence of friction on the sliding rate as well as on other memory effects related to sliding history.

$$\frac{d\theta}{dt} = 1 - \frac{V\theta}{L} \tag{3}$$

where f_* is the reference friction coefficient at the reference slip rate V_*, a and b are rate-and-state parameters, and L is the characteristic slip for the evolution of the state variable. The evolution law of the state variable described by Eq. (3) is the so-called aging law [124–126] and is widely used in the literature. Several other evolution laws have been proposed, including the slip law [126] and the composite law [130,131]. Note that in rate-and-state laws, friction has history-dependent effects, described by the state variable, during changes of slip velocity but becomes solely rate-dependent at constant slip rate and once enough slip has occurred. At steady-state, it takes the form:

$$f_{ss} = f_* + (a - b)\log\left(\frac{V}{V_*}\right) \tag{4}$$

We can use this expression to study the steady-state behavior of our ruptures. Equation (4) is plotted as a straight line in Fig. 9, where the measurements of Fig. 8 are reported (red and blue solid symbols), together with measurements obtained from other experiments [75]. The curve is plotted using the rate-and-state parameters constrained for Homalite by low-velocity experiments [132]: $(a - b) = -0.005$, $f_* = 0.58$, and $V_* = 1\,\mu$m/s.

It is evident that our measurements exhibit a more substantial weakening than that predicted by pure logarithmic rate-and-state friction, which can only produce modest weakening. This suggests the activation of a dynamic weakening mechanism in our experiments resulting in a more pronounced reduction of the friction coefficient. We have found [75] that our measurements are consistent with a combined formulation of rate-and-state laws supplemented with the flash heating formulation [8,133–135] (Fig. 9). Flash
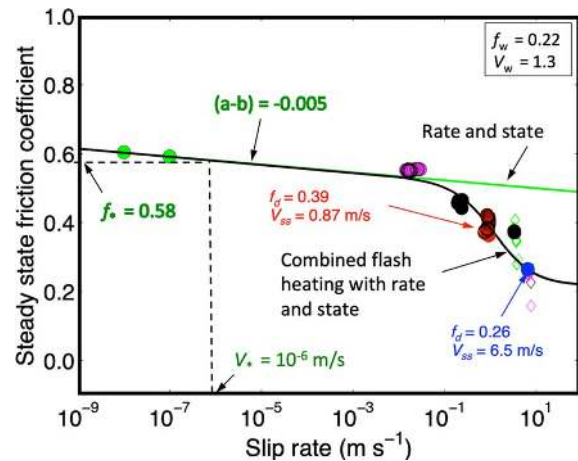
Fig. 9 Experimental measurements of the steady-state friction versus slip rate and fit using the steady-state version of the rate-and-state friction formulation (green curve), and the combined flash heating with rate-and-state friction formulation (black curve, modified from Ref. [75]). Steady-state shear stress and slip rate data are obtained at the trailing edges of each of the ruptures analyzed. The red and blue data points correspond to the two experiments discussed here (presented in Figs. 6 and 7). The fit with the combined flash heating law in this figure only considers the two tests that have the highest accuracy, while the other tests are reported for completeness (experimental conditions detailed in Ref. [75]). Green dots are low-velocity measurements obtained in collaboration with Kilgore, Beeler, and Lu and first reported in Ref. [132]. Our measurements are consistent with the combined formulation of flash heating with rate and state.

heating is a dynamic weakening mechanism in which the contacting asperities heat up and weaken due to the shear motion of the propagating rupture. This produces a marked $1/V$ dependence of friction with slip velocity:

$$f = f_w + (f_0 - f_w)V_w/V \qquad (5)$$

where f_w and V_w are the residual friction coefficient and weakening velocity, respectively, and f_0 is the friction coefficient for $V < V_w$. The weakening velocity V_w is given by [134]

$$V_w = \left(\frac{\pi \alpha_{th}}{D_a}\right)\left[\frac{\rho c_p}{\tau_c}(T_w - T_f)\right]^2 \qquad (6)$$

where α_{th} is the thermal diffusivity, ρc_p is the heat capacity per unit volume, D_a is the average diameter of the contacts, τ_c is the shear strength of the contact (roughly one-tenth of the bulk shear modulus [136]), and $T_w - T_f$ is the temperature change activating flash heating.

In the combined formulation of rate-and-state laws enhanced with flash heating, the coefficient f_0 is replaced by the rate-and-state expression (1) and V is replaced by L/θ [75,137,138]

$$f = f_w^{(c)} + \frac{\left[f_* + a\log\left(\frac{V}{V_*}\right) + b\log\left(\frac{V_*\theta}{L}\right)\right] - f_w^{(c)}}{1 + \frac{L}{\theta V_w^{(c)}}} \qquad (7)$$

where $f_w^{(c)}$ and $V_w^{(c)}$ are the residual friction coefficient and the weakening slip velocity of the combined law, respectively. At steady-state, the state variable evolves into $\theta_{ss} = L/V$, and the steady-state expression of the combined law is

$$f_{ss} = f_w^{(c)} + \frac{\left[f_* + (a-b)\log\left(\frac{V}{V_*}\right)\right] - f_w^{(c)}}{1 + \frac{V}{V_w^{(c)}}} \qquad (8)$$

The steady-state form of the combined friction law provides a good fit to our data (Fig. 9), indicating that our measurements are consistent with the enhanced weakening produced by flash heating. Note that, in Fig. 9, we plot additional steady-state data from several other tests [75], the fit is performed employing only the two tests of Fig. 8. The least-square fit produces $f_w^{(c)} = 0.22$ and $V_w^{(c)} = 1.33$ m/s. The weakening velocity of the standard flash heating mechanism estimated using Eq. (6) is of the order of $V_w = 0.1 - 1$ m/s [75]. While this estimate has some uncertainty as the thermal diffusivity, heat capacity, and shear contact strength of Homalite are not well constrained, it is broadly consistent with the velocity weakening $V_w^{(c)}$ of the combined friction law estimated from the fit.

Our measurements are consistent with the combined friction law of rate and state enhanced with flash heating, but we cannot exclude the activation of other weakening mechanisms. It is not possible to directly observe flash heating in our experiments. Flash heating occurs when tips of contacting asperities (on the order of 1 μm) heat up and weaken. This process is highly transient and does not leave any trace that can be examined after the test has completed. Currently, there is no experimental diagnostic tool that would enable capturing this behavior. Because of these technological and experimental limitations, we can conclude that our measurements are consistent with the combined law of flash heating but we cannot conclusively claim that flash heating is the actual operating weakening mechanism in our experiments.

In order to test whether the rate-and-state and combined friction law can also describe the transient evolution of dynamic friction, we track the friction coefficient predicted by the combined law using the measured slip rate history, including the transient variations associated with the rupture arrival, as input in Eq. (7) and we compare it to the independently measured friction coefficient. Let

us consider as example the rupture studied above, produced with $P = 23$ MPa and $\alpha = 29$ deg, and use the measured slip rate of Fig. 7(a). Equation (6) has two evolving variables, the slip rate V, which we measure, and the state variable θ, which we can compute from the slip rate history, using an evolution law, such as the aging law of Eq. (3). In Eq. (7), we use the rate-and-state parameters $(a - b) = -0.005$, $f_* = 0.58$, and $V_* = 1$ μm/s, constrained by Lu [132] with low-velocity friction experiments, and the combined flash heating parameters $f_w^{(c)} = 0.22$ and $V_w^{(c)} = 1.33$ m/s, obtained from the steady-state fit (Fig. 9). The remaining parameters needed in Eq. (6) are either a or b of rate and state (since their difference is constrained) and the characteristic slip distance L for the evolution variable θ. In order to constrain these two parameters, we develop a least-square procedure minimizing the difference between the estimated friction coefficient via Eq. (2) or (7) and the measured datapoints. The evolution of the state variable is computed recursively using a numerical discretization [139] of Eq. (3): $\theta_{n+1} = \theta_n + (1 - V_n\theta_n/L)\Delta t$, where V_n and θ_n are the values of slip rate and state variable at the time-step n, and Δt is the time-step interval. In order to compute θ recursively, we need an initial value. One route to compute an initial value is to assume steady-state before rupture arrival and compute the initial value of θ as L/V. However, we know from previous measurements [140] that the interface is not in steady-state but it is rather continuously evolving, at very low values of V in the range of $10^{-9} - 10^{-11}$ m/s. Here, we estimate the initial value of the state variable θ_{ini} considering the first measurement of slip rate V_{ini} above the noise floor in combination with the corresponding value of measured friction f_{ini} and inverting Eqs. (2) and (7) for the rate-and-state and combined formulations, respectively. For example, when using the rate-and-state law, θ_{ini} is computed as

$$\theta_{ini} = \frac{L}{V_*}\exp\left(\frac{f_{ini} - f_* - a\log(V_{ini}/V_*)}{b}\right) \qquad (9)$$

where a and L are tentative values. Once the evolution of θ is computed using the discretized form of Eq. (3), its time history is used, together with the slip rate time history, as input in Eq. (2) or (7),

The resulting friction obtained using Eqs. (2) and (7) is plotted versus slip and slip rate in Figs. 10(a) and 10(b), respectively, and it is compared with the measured friction evolution. The comparison shows that the rate-and-state law is able to reproduce the initial strengthening and part of the initial weakening. However, the weakening provided by the rate-and-state law is rather modest and does not capture the full friction reduction displayed by our measurements. Conversely, the combined law provides a good fit to the experimental data, providing an even stronger evidence of our measurements being consistent with the combined rate-and-state friction law enhanced with flash heating. Note that this is an initial attempt to use friction laws to reproduce transient features of the friction measurements, and future work is needed to refine the approach. One aspect to study is whether it is possible to fit multiple tests simultaneously. Considering a collection of tests will challenge existing friction laws and will help to either verify them or propose new ones.

6 Imaging the Formation of Pressure Shock Fronts

The limiting speed of propagating ruptures has been a highly debated topic for several decades [1,5,9,10,18,20–22,141–143]. As we have seen above, shear ruptures can exceed the shear wave speed. When that happens, wavelets emitted at the rupture tip coalesce and give rise to the formation of shear Mach fronts [21,32]. According to singular elastodynamics, shear ruptures propagating in an isotropic solid should not be able to propagate faster than the pressure wave speed. Spontaneously, propagating ruptures are powered by elastodynamic waves, with the energy released by the rupture motion being transferred through the solid at the rupture tip, at the (higher) pressure and (lower) shear wave speed. As a consequence, rupture cannot propagate at a speed faster than the fastest
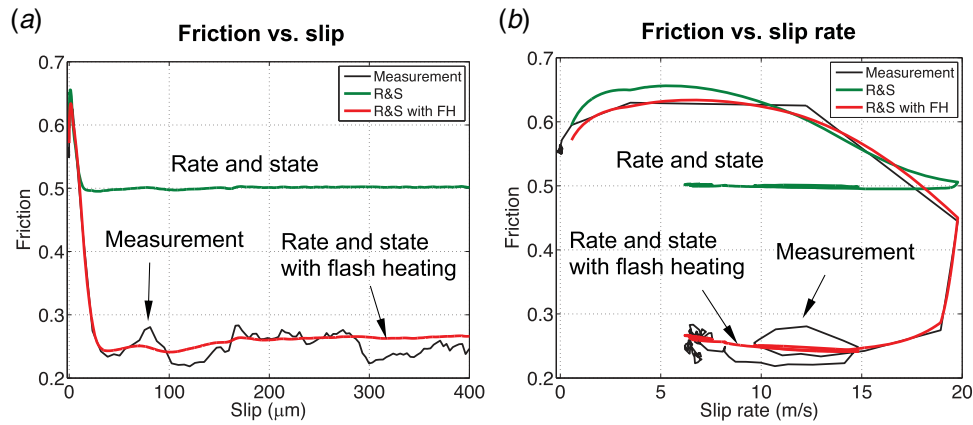
Fig. 10 Fit of the transient experimental measurements of friction employing the standard rate-and-state friction formulation and rate-and-state law enhanced with flash heating (measurements from Ref. [75]). Our measurements are consistent with the rate-and-state friction law supplemented with flash heating, while the standard rate-and-state law alone cannot explain the pronounced weakening observed in the experiments.

way to transfer energy, the pressure wave [1,5,9,10,18]. Since ruptures cannot travel faster than the pressure wave speed, pressure shock fronts should not be able to form.

In a recent study [76], we have observed the formation of pressure shock fronts associated with the spontaneous propagation of shear ruptures in viscoelastic polymers, apparently contradicting classic linear elasticity theory. This contradiction is explained with the high-strain-rate dependence of the polymers inducing local stiffening of the material and locally increasing the effective wave speeds as the crack tip is approached, resulting in the rupture tip propagating slightly less than, or equal to, the local, near-tip pressure wave speed but above the wave speed prevailing in far-field, thus giving rise to the formation of a pressure shock front, in addition to a trailing shear Mach Cone [76]. In other words, the wave speeds, instead of having a single value as in linear elasticity, depending on the local value of the strain rate field at each point, and as such, they exhibit a field variation themselves. In such a case, and if the rupture tip propagates at a speed close to the dynamic (near-tip) p-wave speed, a detached bow shock curved pressure wave shock just ahead of the rupture becomes possible. This is a situation analogous to what happens in gas dynamics [144].

Ruptures are produced in the laboratory setup of Fig. 2, employing specimens made either of Homalite-100 or Polymethyl methacrylate. Numerous tests have been conducted, under various loading and geometrical configuration with both materials, to check the repeatability of results. In the following, we will be discussing tests conducted on Homalite under the following experimental conditions: $P = 25$ Pa and $\alpha = 29$ deg. The full-field maps of particle velocities and strain rates clearly show two sets of shock fronts, a shear and a pressure one (Fig. 11). In order to confirmed that the shock fronts visualized are indeed Mach features, rather than some other manifestation of the corresponding waves, we have verified that the characteristic geometric feature of such fronts (i.e., inclination angle β with respect to the interface) satisfies the kinematic relation characteristic of Mach waves [76]: $\beta = \sin^{-1}(c/V_r)$, where V_r is the measured rupture speed and c is either the pressure or shear wave speed (depending on the front considered). We have explained this behavior by the viscoelastic effects of the polymers resulting in a significant increase in the elastic moduli and effective wave speed with strain rates [76]. The high degree of variability of elastic moduli with strain rates is extensively documented in the literature [145–149]. Using a quasi-elastic approximation [150,151], the material properties can be taken as linear elastic with the effective material constant depending on the local value of strain rate. In this framework, as the strain rate magnitude $|\dot{\varepsilon}|$ increases (Fig. 11(b)), so do the effective wave speeds. The rupture speed, estimated by tracking the rupture tip along the

interface, is nearly constant throughout the field of view and approaches 2.4 km/s, which is higher than both far-field wave speeds of the solid. Note that ruptures propagating at this speed have been observed before [32,49,54,62,63]; however, previous studies did not acknowledge their relevance as they compared the rupture speed to uniformly higher wave speeds and assumed these ruptures were supershear, a well-known phenomenon [9,10,22]. Our work highlights the role of the viscoelastic behavior resulting in spatially heterogeneous stiffening, induced by a highly inhomogeneous field of strain rates, and ultimately in the formation of pressure shock fronts. These observations are enabled by our capability of quantifying the full-field particle velocities, as well as the strain and strain rate tensors.

Shear shock fronts have been visualized in the past by techniques sensitive to the shear deformations, using photoelasticity [10,21,32,62,63] or CGS [33] (Fig. 1), as we have seen in Sec. 2, and can be similarly imaged with DIC [77] (Fig. 4). Since the pressure shock fronts are most visible by imaging quantities sensitive to the dilatational/compressive behavior, it was not possible to observe them before. Using the new ultrahigh-speed DIC technique (Sec. 3, [77]), the pressure shock fronts become clearly visible when plotting the volumetric strain rate tr($\dot{\varepsilon}$) (Fig. 11(c)), while the shear shock fronts are prominent in the shear strain rate $\dot{\varepsilon}_{12}$ [76]. At the crack tip where $|\dot{\varepsilon}|$ is the highest, the effective wave speeds are higher compared with the undeformed solid in the bulk, and the rupture speed can approach this higher limit. In the far-field, where much lower levels of $|\dot{\varepsilon}|$ are attained, wave speeds are lower, so the rupture can propagate at a speed that is higher compared with the pressure wave speed prevailing in the far-field, giving rise to the formation of characteristic shock fronts. In this sense, ruptures can become globally "supersonic." The sequence of fault-parallel velocity (Fig. 11(a)) indicates that the shear shock front is well developed even in the early stages of rupture propagation (e.g., $t = 26.5\ \mu$s in Fig. 11), while the pressure shock front has not fully formed since the strain rate magnitude field is not well established yet. As the strain rate magnitude increases (e.g., $t \geq 47.5\ \mu$s in Fig. 11(b)), it induces a higher contrast of wave speeds and the pressure shock front develops to maturity, as shown by the fault-parallel velocity and volumetric strain rate fields (Figs. 11(a) and 11(c)). While the field of view adopted in Fig. 11 well represents the behavior in the far-field and the formation of shock features, as it was pointed out in Sec. 3 and Fig. 6, such a large field of view is not able to capture the maximum magnitude of the strain rate (Figs. 12(a) and 12(c)). In order to better quantify the level of strain rate magnitude $|\dot{\varepsilon}|$ attained in the near-tip region (Figs. 12(b) and 12(d)), we employ a smaller field of view (inset of Fig. 2).
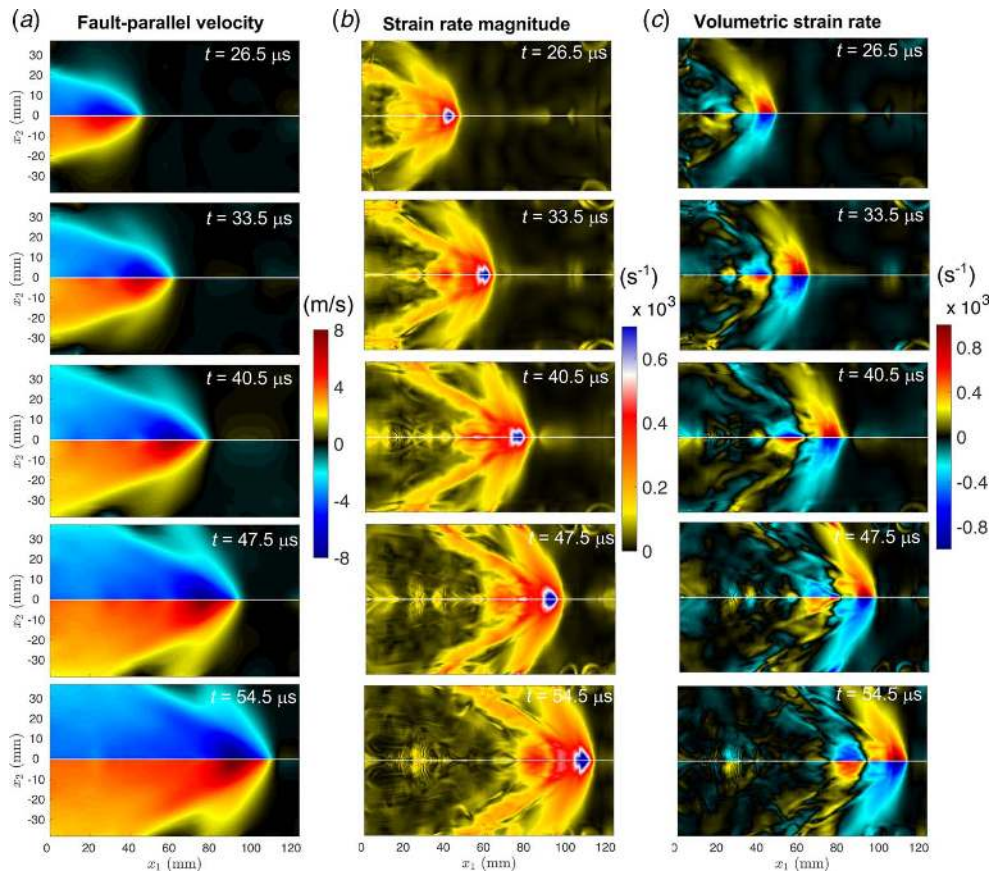
Fig. 11 Formation of pressure shock fronts in Homalite-100, a high-strain rate sensitive material: (a) particle velocity in the fault-parallel direction $\dot{u}_1$, (b) strain rate magnitude $|\dot{\varepsilon}|$, and (c) volumetric strain rate tr($\dot{\varepsilon}$) (figure produced using the data from Ref. [76]). The sequence shows that the pressure shock front fully developing as the strain rate magnitude increases.
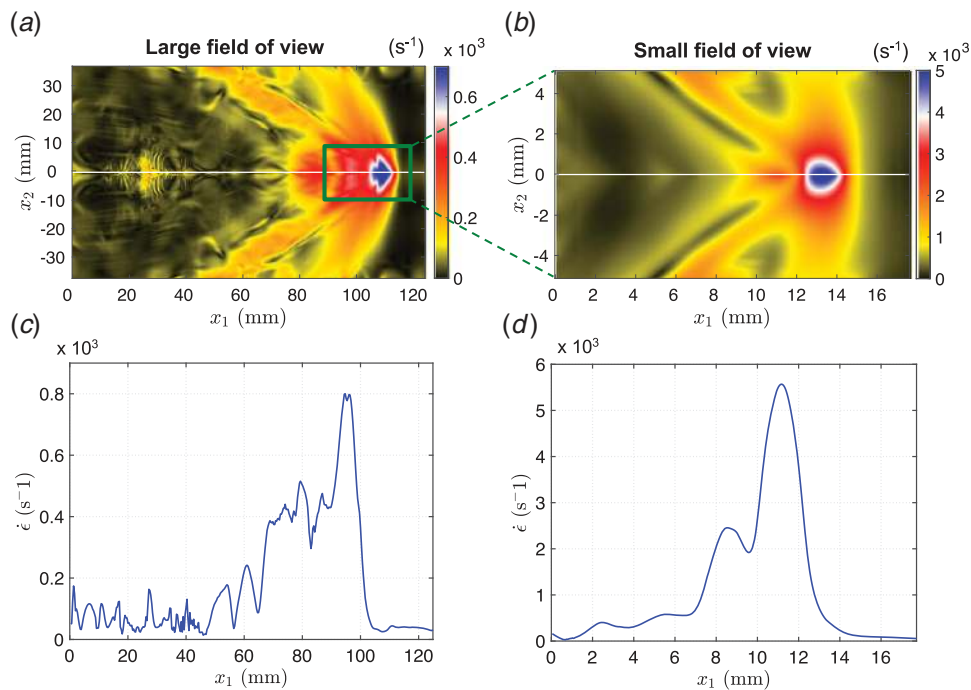
Fig. 12 Strain rate magnitude $|\dot{\varepsilon}|$, obtained with (a) large (124 × 75.4 mm^2) and (b) small (17.6 × 10.4 mm^2) field of view. Strain rate magnitude traced along the interface for the large (c) and small (d) fields of view. The large field of view is used to display features extending in the far-field, while the small field of view is used to quantify the strain rate magnitude attained in the near-tip field.

7 Estimating Out-Plane Displacements and Velocities: Toward Applying 3D-Digital Image Correlation to In-Plane Shear Ruptures

So far, we have discussed the measurements of the in-plane components of displacement and velocity, obtained using a 2D-DIC approach based on a single camera system. Direct measurements of the out-of-plane components would require a stereo-vision system and a 3D-DIC analysis [66]. As a first approximation, we can estimate the out-of-plane displacement component using the measured in-plane displacements and strains and assuming plane-stress conditions. The free-surface condition requires $\sigma_{33}(x_1, x_2, \pm h/2) = 0$. Due to the small thickness of the specimen ($h = 10$ mm) compared with its in-plane dimensions (200×200 mm²), one can assume the plane-stress condition $\partial(\cdot)/\partial x_3 = 0$ and therefore $\sigma_{33}(x_1, x_2, x_3) = 0$ for any $-h/2 \leq x_3 \leq h/2$. This assumption may not strictly hold in our experiments, as a 3D state of stress can develop within the specimen thickness especially at in-plane distances less than a quarter to half the plate thickness [152]. However, the plane-stress approximation can be used to provide a first-order estimate of the out-of-plane displacements and velocities.

The out-of-plane strain $\varepsilon_{33}(x_1, x_2, x_3)$ can be expressed, under a 3D state of stress, as a function of the stress components as $\varepsilon_{33} = -\nu/E(\sigma_{11} + \sigma_{22}) + \sigma_{33}/E$, where ν and E are the Poisson's ratio and Young's modulus, respectively. Under the plane-stress assumption, the out-of-plane strain becomes $\varepsilon_{33}(x_1, x_2) = -\nu/E(\sigma_{11} + \sigma_{22})$ for any $-h/2 \leq x_3 \leq h/2$. The out-of-plane displacement at $x_3 = \pm h/2$ is obtained by integrating ε_{33} through the half-thickness as: $u_{33}(x_1, x_2) = -\nu h/2E (\sigma_{11} + \sigma_{22})$, and the out-of-plane velocity is simply its time derivative, calculated at the frame t_k using a central difference scheme, as $\dot{u}_3(x_1, x_2, t_k) = (\dot{u}_3(x_1, x_2, t_{k+1}) - \dot{u}_3(x_1, x_2, t_{k-1}))/(t_{k+1} - t_{k-1})$. The in-plane stress components, σ_{11} and σ_{22}, are also computed using the plane-stress assumption, e.g., $\sigma_{11} = E/(1 - \nu^2) (\varepsilon_{11} + \nu \varepsilon_{22})$. Note that this expression is strictly valid on the free surfaces $x_3 = \pm h/2$, where $\sigma_{33}(x_1, x_2, \pm h/2) = 0$, even when the plane-stress assumption does not hold through the thickness. The out-of-plane displacement and velocity fields at $x_3 = \pm h/2$ can be expressed as a function of the strain and strain-rate fields as $u_{33}(x_1, x_2) = -\nu h/2(1 - \nu) (\varepsilon_{11} + \varepsilon_{22})$ and $\dot{u}_{33}(x_1, x_2) = -\nu h/2(1 - \nu) (\dot{\varepsilon}_{11} + \dot{\varepsilon}_{22})$, respectively.

The out-of-plane displacements and velocities are shown in Fig. 13 for three different rupture scenarios: a sub-Rayleigh rupture propagating at $V_r < c_R^{HSR}$ (Figs. 13(a) and 13(b)), a
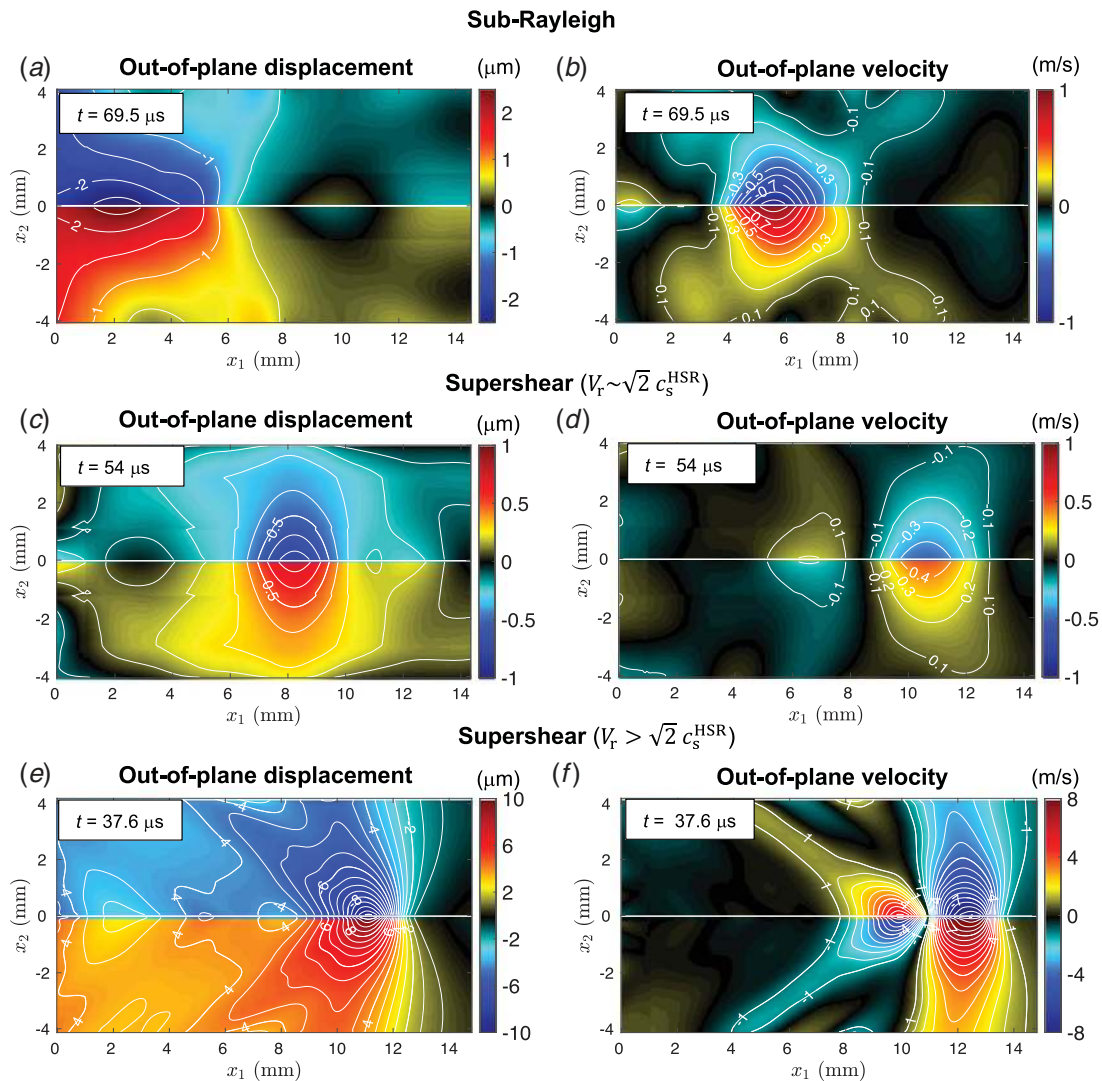
Fig. 13 Estimated out-of-plane displacements (left) and velocity (right) of the (a) and (b) sub-Rayleigh rupture and of the two supershear ruptures traveling at (c) and (d) $V_r \sim \sqrt{2} \, c_s^{HSR}$ and (e) and (f) $V_r > \sqrt{2} \, c_s^{HSR}$, respectively. The out-of-plane displacement and velocity are estimated from in-plane, surface, measurements under the plane-stress assumption. While this assumption may not strictly hold for the present ruptures, these estimates give an order of magnitude for the out-of-plane full-field displacements and velocities.

supershear rupture propagating at $V_r \sim \sqrt{2}\, c_s^{HSR}$ (Figs. 13(c) and 13(d)), and a supershear rupture propagating at $V_r > \sqrt{2}\, c_s^{HSR}$ (Figs. 13(e) and 13(f)). These three cases correspond to three different experiments featuring: (1) $P = 12$ MPa and $\alpha = 24$ deg, (2) $P = 4.5$ MPa and $\alpha = 29$ deg, and (3) $P = 23$ Pa and $\alpha = 29$ deg, respectively. These in-plane components of these ruptures are discussed in Ref. [153]. Note that the supershear rupture of Figs. 13(a) and 13(b) is the same rupture shown here in Fig. 5. The maximum values of the out-of-plane displacements are smaller when compared with the in-plane components. For example, the sub-Raleigh rupture has maximum in-plane displacements on the order of 15 μm [153], while the estimated out-of-plane component is on the order of 2 μm. For the case of the supershear rupture propagating at $V_r > \sqrt{2}\, c_s^{HSR}$, the fault-parallel displacement component is on the order of 50 μm at a time $t = 37.6$ μs after rupture nucleation, and it occurs behind the rupture tip where slip accumulates. At the same time after nucleation, the maximum estimated out-of-plane displacement is $u_3 \sim 10\,\mu$m and occurs near the rupture tip (Fig. 13(e)), where the fault-parallel strain ε_{11}, the dominant strain component in the expression of u_3, is maximum [77]. Note that the out-of-plane motion can compromise the in-plane measurements. In-plane strain errors due to out-of-plane translation scale with $\Delta Z/Z$, where Z is the stand-off distance, i.e., the distance between the camera and the specimen, and $\Delta Z = u_3$ is the change of stand-off distance associated with the out-of-plane displacement [66]. In-plane strain errors due to the out-of-plane rotation depend on both the rotation angle and the stand-off distance Z [66]. In our setup, featuring one high-speed camera with its axis perpendicular to the specimen, Z is on the order of several 100 s mm whereas ΔZ is on the order of microns, so out-of-plane motion has no significant effect on the measurement of in-plane quantities.

In contrast with the out-plane displacements, the out-of-plane velocity components are of the same order of magnitude as the in-plane components. For the sub-Rayleigh rupture, the maximum of each of the in-plane velocity components is $\dot{u}_1^{max} \sim 1$ m/s and $\dot{u}_2^{max} \sim 2.5$ m/s, respectively (Figs. 4(a) and 5(a)), while the maximum of out-of-plane velocity is $\dot{u}_3^{max} \sim 1$ m/s (Fig. 13(b)). For the supershear rupture propagating at the special speed of $V_r \sim \sqrt{2}\, c_s^{HSR}$, the maximum out-of-plane velocity is $\dot{u}_3^{max} \sim 1$ m/s (Fig. 13(d)) and is also comparable to the in-plane components. For the stronger supershear rupture, propagating at $V_r > \sqrt{2}\, c_s^{HSR}$, the maximum out-of-plane velocity is $\dot{u}_3^{max} \sim 10$ m/s (Fig. 13(f)). Both are of the same order of magnitude as their fault-parallel velocity components [153]. To summarize, this analysis indicates that (i) the out-of-plane velocities are more important than the out-of-plane displacements when compared with the respective in-plane components and (ii) the out-of-plane velocities are much more important for strong supershear ruptures $(V_r > \sqrt{2}\, c_s^{HSR})$ than they are for sub-Rayleigh or supershear ruptures propagating at the Eshelby speed, which has important implications for ground motion scenarios associated with these types of earthquakes.

In order to directly measure the out-of-plane displacements, an ultrahigh-speed stereo-vision system and 3D-DIC analysis are required. While we are planning to perform these measurements in future studies, our initial computation of out-of-plane displacements and velocities assuming plane stress and using the measured in-plane displacements provide an order of magnitude estimate, useful to gain insight into the out-of-plane fields. These estimates underline the importance of the out-of-plane components and motivate future experiments including diagnostics for 3D measurements. These measurements will also help to quantify the discrepancy between the plane-stress state assumed here and the 3D state of stress developing through the specimen's thickness.

8 Conclusions

Several important developments have changed the face of experimental fracture mechanics over the last few decades. In our laboratory, the development of the new generation of the "Laboratory Earthquake" setup involving ultrahigh-speed digital image correlation has brought in a revolution by allowing us to quantify the full-field temporal evolution of dynamic ruptures in both transparent and opaque solids and by uncovering extraordinary behaviors that could not be to visualized until very recently. The measurements enabled by DIC are consistent with previous photoelasticity and velocimeter measurements but allow us to quantify full fields, including all strain and stress components. The velocity-time histories obtained with DIC can be produced for any point in the field of view and are equivalent to velocimeter measurements, which we previously employed in our laboratory setup but that could only be performed only up to three locations per test. In particular, the following milestones have been achieved:

(1) Being able to produce these velocity measurements over a dense spatial domain at the vicinity of the fault is an invaluable advancement in the capability to monitor the ground shaking signatures of dynamically propagating ruptures and is equivalent of having almost an unlimited number of seismometers in the field.

(2) Measuring the local evolution of dynamic friction is a key milestone in the study of shear ruptures. We have developed a non-conventional methodology to study friction without imposing slip-velocity histories to the sliding interface or assuming uniform sliding, but rather by tracking how friction evolves in spontaneously propagating ruptures. These measurements will allow us to verify the capability of current history-dependent friction formulations to accurately describe a wide range of behaviors and to potentially improve the formulations.

(3) We have also been able to uncover new phenomena, such as the apparent "supersonic" growth of shear cracks in viscoelastic solids and the associated formation of curved pressure shock fronts associated with the spontaneous propagation of shear ruptures in such materials, apparently contradicting classical theories. This unexpected behavior is explained by recognizing and quantifying the field dependence of the stress waves speeds on the local strain rate field induced by the growing rupture tip The new technique allowed us to measure both the highly heterogeneous strain rate fields responsible for this behavior, and the volumetric strain rates and shear strain rates clearly displaying the formation of the pressure as well as the shear shock fronts.

(4) We have been able to estimate out-of-plane displacement and velocity fields on the free specimen surface by using in-plane fields and the assumption of plane stress. These estimates indicate that the out-of-plane velocities are of the same order of magnitude as the in-plane velocities for shear ruptures. Both out-of-plane displacements and velocities are particularly large for the case of strong supershear ruptures when compared with slower supershear or sub-Rayleigh ruptures. While these observations need to be confirmed by fully 3D measurements employing a stereo-vision system, which will be the subject of future studies, these preliminary results give important insights into the potential ground motion associated with the out-of-plane component.

References

[1] Freund, L. B., 1998, *Dynamic Fracture Mechanics*, Cambridge University Press, Cambridge.

[2] Broberg, K. B., 1999, *Cracks and Fracture*, Elsevier, New York.

[3] Das, S., 1985, "Application of Dynamic Shear Crack Models to the Study of the Earthquake Faulting Process," *Dynamic Fracture*, Springer, New York, pp. 137–150.

[4] Dmowska, R., and Rice, J., 1986, "Fracture Theory and Its Seismological Applications," *Continuum Theories in Solid Earth Physics*, R. Teisseyre, ed., Polish Scientific, Warsaw, pp. 187–255.

[5] Rice, J. R., 2001, "New Perspectives on Crack and Fault Dynamics," *Mechanics for a New Millennium*, Springer, New York, pp. 1–24.

[6] Scholz, C. H., 2019, *The Mechanics of Earthquakes and Faulting*, Cambridge University Press, Cambridge.

[7] Fialko, Y., 2006, "Interseismic Strain Accumulation and the Earthquake Potential on the Southern San Andreas Fault System," Nature, **441**(7096), pp. 968–971.

[8] Tullis, T. E., 2015, *Treatise on Geophysics*, 2nd ed., Elsevier, Oxford, pp. 139–159.

[9] Rosakis, A. J., 2002, "Intersonic Shear Cracks and Fault Ruptures," Adv. Phys., **51**(4), pp. 1189–1257.

[10] Rosakis, A. J., Xia, K., Lykotrafitis, G., and Kanamori, H., 2007, "Dynamic Shear Rupture in Frictional Interfaces-Speeds, Directionality, and Modes," *Treatise on Geophysics*, Elsevier, New York, pp. 153–192.

[11] Cotterell, B., and Rice, J., 1980, "Slightly Curved or Kinked Cracks," Int. J. Fract., **16**(2), pp. 155–169.

[12] Nemat-Nasser, S., and Horii, H., 1982, "Compression-Induced Nonplanar Crack Extension With Application to Splitting, Exfoliation, and Rockburst," J. Geophys. Res. Solid Earth, **87**(B8), pp. 6805–6821.

[13] Hutchinson, J. W., and Suo, Z., 1991, "Mixed Mode Cracking in Layered Materials," Adv. Appl. Mech., **29**, pp. 63–191.

[14] Melin, S., 1986, "When Does a Crack Grow Under Mode II Conditions?" Int. J. Fract., **30**(2), pp. 103–114.

[15] Broberg, K., 1987, "On Crack Paths," Eng. Fract. Mech., **28**(5–6), pp. 663–679.

[16] Yao, W., Xu, Y., Yu, C., and Xia, K., 2017, "A Dynamic Punch-Through Shear Method for Determining Dynamic Mode II Fracture Toughness of Rocks," Eng. Fract. Mech., **176**, pp. 161–177.

[17] Xu, Y., Yao, W., Zhao, G., and Xia, K., 2019, "Evaluation of the Short Core in Compression (SCC) Method for Measuring Mode II Fracture Toughness of Rocks," Eng. Fract. Mech., p. 106747.

[18] Needleman, A., 1999, "An Analysis of Intersonic Crack Growth Under Shear Loading," ASME J. Appl. Mech., **66**(4), pp. 847–857.

[19] Gao, H., Huang, Y., Gumbsch, P., and Rosakis, A., 1999, "On Radiation-Free Transonic Motion of Cracks and Dislocations," J. Mech. Phys. Solids, **47**(9), pp. 1941–1961.

[20] Abraham, F. F., and Gao, H., 2000, "How Fast can Cracks Propagate?" Phys. Rev. Lett., **84**(14), p. 3113.

[21] Xia, K., Rosakis, A. J., and Kanamori, H., 2004, "Laboratory Earthquakes: The Sub-Rayleigh-to-Supershear Rupture Transition," Science, **303**(5665), pp. 1859–1861.

[22] Fineberg, J., and Bouchbinder, E., 2015, "Recent Developments in Dynamic Fracture: Some Perspectives," Int. J. Fract., **196**(1–2), pp. 33–57.

[23] Broberg, K., 1996, "How Fast Can a Crack go?," Mater. Sci., **32**(1), pp. 80–86.

[24] Rosakis, A., and Huang, Y., 2003, *Comprehensive Structural Integrity Handbook, Fracture of Materials From Nano to Macro*, Elsevier Ltd, Oxford, pp. 137–179.

[25] Tippur, H., and Rosakis, A., 1991, "Quasi-Static and Dynamic Crack Growth Along Bimaterial Interfaces: A Note on Crack-Tip Field Measurements Using Coherent Gradient Sensing," Exp. Mech., **31**(3), pp. 243–251.

[26] Lambros, J., and Rosakis, A. J., 1995, "Dynamic Decohesion of Bimaterials: Experimental Observations and Failure Criteria," Int. J. Solids Struct., **32**(17–18), pp. 2677–2702.

[27] Singh, R., and Shukla, A., 1996, "Subsonic and Intersonic Crack Growth Along a Bimaterial Interface," J. Appl. Mech., **63**(4), pp. 919–924.

[28] Singh, R. P., Lambros, J., Shukla, A., and Rosakis, A. J., 1997, "Investigation of the Mechanics of Intersonic Crack Propagation Along a Bimaterial Interface Using Coherent Gradient Sensing and Photoelasticity," Philos. Trans. R. Soc. London, Ser. A, **453**(1967), pp. 2649–2667.

[29] Samudrala, O., and Rosakis, A., 2003, "Effect of Loading and Geometry on the Subsonic/Intersonic Transition of a Bimaterial Interface Crack," Eng. Fract. Mech., **70**(2), pp. 309–337.

[30] Huang, Y., Wang, W., Liu, C., and Rosakis, A., 1998, "Intersonic Crack Growth in Bimaterial Interfaces: An Investigation of Crack Face Contact," J. Mech. Phys. Solids, **46**(11), pp. 2233–2259.

[31] Wang, W., Huang, Y., Rosakis, A., and Liu, C., 1998, "Effect of Elastic Mismatch in Intersonic Crack Propagation Along a Bimaterial Interface," Eng. Fract. Mech., **61**(5–6), pp. 471–485.

[32] Rosakis, A., Samudrala, O., and Coker, D., 1999, "Cracks Faster Than the Shear Wave Speed," Science, **284**(5418), pp. 1337–1340.

[33] Coker, D., and Rosakis, A. J., 2001, "Experimental Observations of Intersonic Crack Growth in Asymmetrically Loaded Unidirectional Composite Plates," Philos. Mag. A, **81**(3), pp. 571–595.

[34] Huang, Y., Wang, W., Liu, C., and Rosakis, A., 1999, "Analysis of Intersonic Crack Growth in Unidirectional Fiber-Reinforced Composites," J. Mech. Phys. Solids, **47**(9), pp. 1893–1916.

[35] Archuleta, R. J., 1984, "A Faulting Model for the 1979 Imperial Valley Earthquake," J. Geophys. Res. Solid Earth, **89**(B6), pp. 4559–4585.

[36] Spudich, P., and Cranswick, E., 1984, "Direct Observation of Rupture Propagation During the 1979 Imperial Valley Earthquake Using a Short Baseline Accelerometer Array," Bull. Seismol. Soc. Am., **74**(6), pp. 2083–2114.

[37] Olsen, K., Madariaga, R., and Archuleta, R. J., 1997, "Three-dimensional Dynamic Simulation of the 1992 Landers Earthquake," Science, **278**(5339), pp. 834–838.

[38] Burridge, R., 1973, "Admissible Speeds for Plane-Strain Self-Similar Shear Cracks With Friction but Lacking Cohesion," Geophys. J. Int., **35**(4), pp. 439–455.

[39] Andrews, D., 1976, "Rupture Velocity of Plane Strain Shear Cracks," J. Geophys. Res. Solid Earth, **81**(32), pp. 5679–5687.

[40] Coker, D., Lykotrafitis, G., Needleman, A., and Rosakis, A., 2005, "Frictional Sliding Modes Along an Interface Between Identical Elastic Plates Subject to Shear Impact Loading," J. Mech. Phys. Solids, **53**(4), pp. 884–922.

[41] Bouchon, M., Bouin, M. P., Karabulut, H., Toksöz, M. N., Dietrich, M., and Rosakis, A. J., 2001, "How Fast is Rupture During an Earthquake? New Insights From the 1999 Turkey Earthquakes," Geophys. Res. Lett., **28**(14), pp. 2723–2726.

[42] Bouchon, M., and Vallée, M., 2003, "Observation of Long Supershear Rupture During the Magnitude 8.1 Kunlunshan Earthquake," Science, **301**(5634), pp. 824–826.

[43] Ellsworth, W., Celebi, M., Evans, J., Jensen, E., Kayen, R., Metz, M., Nyman, D., Roddick, J., Spudich, P., and Stephens, C., 2004, "Near-Field Ground Motion of the 2002 Denali Fault, Alaska, Earthquake Recorded at Pump Station 10," Earthquake spectra, **20**(3), pp. 597–615.

[44] Song, S. G., Beroza, G. C., and Segall, P., 2008, "A Unified Source Model for the 1906 San Francisco Earthquake," Bull. Seismol. Soc. Am., **98**(2), pp. 823–831.

[45] Bao, H., Ampuero, J.-P., Meng, L., Fielding, E. J., Liang, C., Milliner, C. W., Feng, T., and Huang, H., 2019, "Early and Persistent Supershear Rupture of the 2018 Magnitude 7.5 Palu Earthquake," Nat. Geosci., **12**(3), pp. 200–205.

[46] Rubinstein, S. M., Cohen, G., and Fineberg, J., 2004, "Detachment Fronts and the Onset of Dynamic Friction," Nature, **430**(7003), p. 1005.

[47] Dunham, E. M., 2007, "Conditions Governing the Occurrence of Supershear Ruptures Under Slip-Weakening Friction," J. Geophys. Res. Solid Earth, **112**(B7).

[48] Liu, Y., and Lapusta, N., 2008, "Transition of Mode II Cracks From Sub-Rayleigh to Intersonic Speeds in the Presence of Favorable Heterogeneity," J. Mech. Phys. Solids, **56**(1), pp. 25–50.

[49] Ben-David, O., Cohen, G., and Fineberg, J., 2010, "The Dynamics of the Onset of Frictional Slip," Science, **330**(6001), pp. 211–214.

[50] Schubnel, A., Nielsen, S., Taddeucci, J., Vinciguerra, S., and Rao, S., 2011, "Photo-Acoustic Study of Subshear and Supershear Ruptures in the Laboratory," Earth Planet. Sci. Lett., **308**(3–4), pp. 424–432.

[51] Passelegue, F. X., Schubnel, A., Nielsen, S., Bhat, H. S., and Madariaga, R., 2013, "From Sub-Rayleigh to Supershear Ruptures During Stick-Slip Experiments on Crustal Rocks," Science, **340**(6137), pp. 1208–1211.

[52] Svetlizky, I., and Fineberg, J., 2014, "Classical Shear Cracks Drive the Onset of dry Frictional Motion," Nature, **509**(7499), p. 205.

[53] Bayart, E., Svetlizky, I., and Fineberg, J., 2016, "Fracture Mechanics Determine the Lengths of Interface Ruptures That Mediate Frictional Motion," Nat. Phys., **12**(2), pp. 166–170.

[54] Svetlizky, I., Bayart, E., Cohen, G., and Fineberg, J., 2017, "Frictional Resistance Within the Wake of Frictional Rupture Fronts," Phys. Rev. Lett., **118**(23), p. 234301.

[55] Kammer, D. S., Svetlizky, I., Cohen, G., and Fineberg, J., 2018, "The Equation of Motion for Supershear Frictional Rupture Fronts," Sci. Adv., **4**(7), p. eaat5622.

[56] Xia, K., Rosakis, A. J., Kanamori, H., and Rice, J. R., 2005, "Laboratory Earthquakes Along Inhomogeneous Faults: Directionality and Supershear," Science, **308**(5722), pp. 681–684.

[57] Biegel, R. L., Sammis, C. G., and Rosakis, A. J., 2008, "An Experimental Study of the Effect of off-Fault Damage on the Velocity of a Slip Pulse," J. Geophys. Res. Solid Earth, **113**(B4).

[58] Bhat, H. S., Biegel, R. L., Rosakis, A. J., and Sammis, C. G., 2010, "The Effect of Asymmetric Damage on Dynamic Shear Rupture Propagation II: With Mismatch in Bulk Elasticity," Tectonophysics, **493**(3–4), pp. 263–271.

[59] Lu, X., Lapusta, N., and Rosakis, A. J., 2007, "Pulse-Like and Crack-Like Ruptures in Experiments Mimicking Crustal Earthquakes," Proc. Natl. Acad. Sci. U.S.A., **104**(48), pp. 18931–18936.

[60] Lu, X., Rosakis, A. J., and Lapusta, N., 2010, "Rupture Modes in Laboratory Earthquakes: Effect of Fault Prestress and Nucleation Conditions," J. Geophys. Res. Solid Earth, **115**(B12).

[61] Ngo, D., Huang, Y., Rosakis, A., Griffith, W., and Pollard, D., 2012, "Off-Fault Tensile Cracks: A Link Between Geological Fault Observations, Lab Experiments, and Dynamic Rupture Models," J. Geophys. Res. Solid Earth, **117**(B1).

[62] Mello, M., Bhat, H. S., Rosakis, A. J., and Kanamori, H., 2010, "Identifying the Unique Ground Motion Signatures of Supershear Earthquakes: Theory and Experiments," Tectonophysics, **493**(3–4), pp. 297–326.

[63] Mello, M., Bhat, H. S., and Rosakis, A. J., 2016, "Spatiotemporal Properties of Sub-Rayleigh and Supershear Rupture Velocity Fields: Theory and Experiments," J. Mech. Phys. Solids, **93**, pp. 153–181.

[64] Gabuchian, V., Rosakis, A. J., Lapusta, N., and Oglesby, D. D., 2014, "Experimental Investigation of Strong Ground Motion Due to Thrust Fault Earthquakes," J. Geophys. Res. Solid Earth, **119**(2), pp. 1316–1336.

[65] Gabuchian, V., Rosakis, A. J., Bhat, H. S., Madariaga, R., and Kanamori, H., 2017, "Experimental Evidence That Thrust Earthquake Ruptures Might Open Faults," Nature, **545**(7654), p. 336.

[66] Sutton, M. A., Orteu, J. J., and Schreier, H., 2009, *Image Correlation for Shape, Motion and Deformation Measurements: Basic Concepts, Theory and Applications*, Springer, New York, NY.

[67] Sutton, M., Matta, F., Rizos, D., Ghorbani, R., Rajan, S., Mollenhauer, D., Schreier, H., and Lasprilla, A., 2017, "Recent Progress in Digital Image Correlation: Background and Developments Since the 2013 WM Murray Lecture," Exp. Mech., **57**(1), pp. 1–30.

[68] Hild, F., and Roux, S., 2012, *Digital Image Correlation*, Wiley-VCH, Weinheim.

[69] Hild, F., and Roux, S., 2012, "Comparison of Local and Global Approaches to Digital Image Correlation," Exp. Mech., **52**(9), pp. 1503–1519.

[70] Wang, B., and Pan, B., 2016, "Subset-Based Local vs. Finite Element-Based Global Digital Image Correlation: a Comparison Study," Theor. Appl. Mech. Lett., **6**(5), pp. 200–208.

[71] Sutton, M., Wolters, W., Peters, W., Ranson, W., and McNeill, S., 1983, "Determination of Displacements Using an Improved Digital Correlation Method," Image Vision Comput., **1**(3), pp. 133–139.

[72] Sutton, M., Mingqi, C., Peters, W., Chao, Y., and McNeill, S., 1986, "Application of an Optimized Digital Correlation Method to Planar Deformation Analysis," Image Vision Comput., **4**(3), pp. 143–150.

[73] Sun, Y., Pang, J. H., Wong, C. K., and Su, F., 2005, "Finite Element Formulation for a Digital Image Correlation Method," Appl. Opt., **44**(34), pp. 7357–7363.

[74] Besnard, G., Hild, F., and Roux, S., 2006, ""Finite-Element" Displacement Fields Analysis From Digital Images: Application to Portevin–Le Châtelier Bands," Exp. Mech., **46**(6), pp. 789–803.

[75] Rubino, V., Rosakis, A., and Lapusta, N., 2017, "Understanding Dynamic Friction Through Spontaneously Evolving Laboratory Earthquakes," Nat. Commun., **8**, p. 15991.

[76] Gori, M., Rubino, V., Rosakis, A., and Lapusta, N., 2018, "Pressure Shock Fronts Formed by Ultra-Fast Shear Cracks in Viscoelastic Materials," Nat. Commun., **9**(1), p. 4754.

[77] Rubino, V., Rosakis, A., and Lapusta, N., 2019, "Full-Field Ultrahigh-Speed Quantification of Dynamic Shear Ruptures Using Digital Image Correlation," Exp. Mech., **59**(5), pp. 1–32.

[78] Tal, Y., Rubino, V., Rosakis, A. J., and Lapusta, N., 2019, "Enhanced Digital Image Correlation Analysis of Ruptures with Enforced Traction Continuity Conditions Across Interfaces," Appl. Sci., **9**(8), p. 1625.

[79] Rubino, V., Lapusta, N., Rosakis, A. J., Leprince, S., and Avouac, J. P., 2015, "Static Laboratory Earthquake Measurements with the Digital Image Correlation Method," Exp. Mech., **55**(1), pp. 77–94.

[80] Michel, R., Ampuero, J.-P., Avouac, J.-P., Lapusta, N., Leprince, S., Redding, D., and Somala, S., 2012, "A Geostationary Optical Seismometer, Proof of Concept," IEEE Trans. Geosci. Remote Sens., **51**(1), pp. 695–703.

[81] Cruikshank, K. M., Zhao, G., and Johnson, A. M., 1991, "Analysis of Minor Fractures Associated With Joints and Faulted Joints," J. Struct. Geol., **13**(8), pp. 865–886.

[82] Rispoli, R., 1981, "Stress Fields About Strike-Slip Faults Inferred From Stylolites and Tension Gashes," Tectonophysics, **75**(3–4), pp. T29–T36.

[83] Willemse, E. J., Peacock, D. C., and Aydin, A., 1997, "Nucleation and Growth of Strike-Slip Faults in Limestones From Somerset, UK," J. Struct. Geol., **19**(12), pp. 1461–1477.

[84] Martel, S. J., and Boger, W. A., 1998, "Geometry and Mechanics of Secondary Fracturing Around Small Three-Dimensional Faults in Granitic Rock," J. Geophys. Res. Solid Earth, **103**(B9), pp. 21299–21314.

[85] Cooke, M., Mollema, P., Pollard, D., and Aydin, A., 2000, "Interlayer Slip and Fracture Clusters Within East Kaibab Monocline: Numerical Analysis and Field Investigations," J. Geol. Soc. London, **169**, pp. 23–49.

[86] Kattenhorn, S. A., Aydin, A., and Pollard, D. D., 2000, "Joints at High Angles to Normal Fault Strike: An Explanation Using 3-D Numerical Models of Fault-Perturbed Stress Fields," J. Struct. Geol., **22**(1), pp. 1–23.

[87] Kattenhorn, S. A., and Marshall, S. T., 2006, "Fault-Induced Perturbed Stress Fields and Associated Tensile and Compressive Deformation at Fault Tips in the ice Shell of Europa: Implications for Fault Mechanics," J. Struct. Geol., **28**(12), pp. 2204–2221.

[88] Barthelat, F., Wu, Z., Prorok, B., and Espinosa, H., 2003, "Dynamic Torsion Testing of Nanocrystalline Coatings Using High-Speed Photography and Digital Image Correlation," Exp. Mech., **43**(3), pp. 331–340.

[89] Kirugulige, M. S., Tippur, H. V., and Denney, T. S., 2007, "Measurement of Transient Deformations Using Digital Image Correlation Method and High-Speed Photography: Application to Dynamic Fracture," Appl. Opt., **46**(22), pp. 5083–5096.

[90] Kirugulige, M., and Tippur, H., 2009, "Measurement of Fracture Parameters for a Mixed-Mode Crack Driven by Stress Waves Using Image Correlation Technique and High-Speed Digital Photography," Strain, **45**(2), pp. 108–122.

[91] Jajam, K., and Tippur, H., 2011, "An Experimental Investigation of Dynamic Crack Growth Past a Stiff Inclusion," Eng. Fract. Mech., **78**(6), pp. 1289–1305.

[92] Gao, G., Yao, W., Xia, K., and Li, Z., 2015, "Investigation of the Rate Dependence of Fracture Propagation in Rocks Using Digital Image Correlation (DIC) Method," Eng. Fract. Mech., **138**, pp. 146–155.

[93] Gao, G., Huang, S., Xia, K., and Li, Z., 2015, "Application of Digital Image Correlation (DIC) in Dynamic Notched Semi-Circular Bend (NSCB) Tests," Exp. Mech., **55**(1), pp. 95–104.

[94] Koohbor, B., Kidane, A., Sutton, M. A., Zhao, X., and Mallon, S., 2017, "Analysis of Dynamic Bending Test Using Ultra High Speed DIC and the Virtual Fields Method," Int. J. Impact Eng., **110**, pp. 299–310.

[95] Pierron, F., Cheriguene, R., Forquin, P., Moulart, R., Rossi, M., and Sutton, M., 2011, "Performances and Limitations of Three Ultra High-Speed Imaging Cameras for Full-Field Deformation Measurements," Appl. Mech. Mater., **70**, pp. 81–86.

[96] Reu, P. L., "High/Ultra-High Speed Imaging as a Diagnostic Tool," Appl. Mech. Mater., pp. 69–74.

[97] Xing, H., Zhang, Q., Braithwaite, C. H., Pan, B., and Zhao, J., 2017, "High-Speed Photography and Digital Optical Measurement Techniques for Geomaterials: Fundamentals and Applications," Rock Mech. Rock Eng., **50**(6), pp. 1611–1659.

[98] Kondo, Y., Takubo, K., Tominaga, H., Hirose, R., Tokuoka, N., Kawaguchi, Y., Takaie, Y., Ozaki, A., Nakaya, S., and Yano, F., 2012, "Development of "HyperVision HPV-X" High-Speed Video Camera," Shimadzu Rev., **69**, pp. 285–291.

[99] Tochigi, Y., Hanzawa, K., Kato, Y., Kuroda, R., Mutoh, H., Hirose, R., Tominaga, H., Takubo, K., Kondo, Y., and Sugawa, S., 2013, "A Global-Shutter CMOS Image Sensor With Readout Speed of 1-Tpixel/s Burst and 780-Mpixel/s Continuous," IEEE J. Solid-State Circuits, **48**(1), pp. 329–338.

[100] Rubino, V., Lapusta, N., and Rosakis, A., 2012, "Laboratory Earthquake Measurements with the High-Speed Digital Image Correlation Method and Applications to Super-Shear Transition," Proceedings of the AGU Fall Meeting Abstracts., San Francisco, CA, Dec. 3–7.

[101] Rubino, V., Rosakis, A., and Lapusta, N., 2015, "Dynamic Imaging of Strain and Stress Evolution in Laboratory Earthquakes with the Ultra-High-Speed Digital Image Correlation Technique," Proceedings of the AGU Fall Meeting Abstracts, San Francisco, CA, Dec. 14–15.

[102] Buades, A., Coll, B., and Morel, J. M., 2006, "The Staircasing Effect in Neighborhood Filters and its Solution," IEEE Trans. Image Process., **15**(6), pp. 1499–1505.

[103] Buades, A., Coll, B., and Morel, J. M., 2008, "Nonlocal Image and Movie Denoising," Int. J. Comput. Vision, **76**(2), pp. 123–139.

[104] Ayoub, F., Leprince, S., and Keene, L., 2009, *User's Guide to COSI-CORR co-Registration of Optically Sensed Images and Correlation*, California Institute of Technology, Pasadena, CA, p. 38.

[105] Jin, H., and Bruck, H. A., 2005, "Theoretical Development for Pointwise Digital Image Correlation," Opt. Eng., **44**(6), p. 067003.

[106] Réthoré, J., Hild, F., and Roux, S., 2007, "Shear-Band Capturing Using a Multiscale Extended Digital Image Correlation Technique," Comput. Meth. Appl. Mech. Eng., **196**(49–52), pp. 5016–5030.

[107] Réthoré, J., Hild, F., and Roux, S., 2008, "Extended Digital Image Correlation With Crack Shape Optimization," Int. J. Numer. Methods Eng., **73**(2), pp. 248–272.

[108] Poissant, J., and Barthelat, F., 2010, "A Novel 'Subset Splitting' Procedure for Digital Image Correlation on Discontinuous Displacement Fields," Exp. Mech., **50**(3), pp. 353–364.

[109] Nguyen, T. L., Hall, S. A., Vacher, P., and Viggiani, G., 2011, "Fracture Mechanisms in Soft Rock: Identification and Quantification of Evolving Displacement Discontinuities by Extended Digital Image Correlation," Tectonophysics, **503**(1–2), pp. 117–128.

[110] Tomičević, Z., Hild, F., and Roux, S., 2013, "Mechanics-Aided Digital Image Correlation," J. Strain Anal. Eng. Des., **48**(5), pp. 330–343.

[111] Hassan, G. M., MacNish, C., and Dyskin, A., "Extending Digital Image Correlation to Reconstruct Displacement and Strain Fields Around Discontinuities in Geomechanical Structures Under Deformation," 2015 IEEE Winter Conference on the Proceedings of the Applications of Computer Vision (WACV), IEEE, New York, pp. 710–717.

[112] Lykotrafitis, G., Rosakis, A. J., and Ravichandran, G., 2006, "Particle Velocimetry and Photoelasticity Applied to the Study of Dynamic Sliding Along Frictionally-Held Bimaterial Interfaces: Techniques and Feasibility," Exp. Mech., **46**(2), pp. 205–216.

[113] Fialko, Y., 2015, "Fracture and Frictional Mechanics: Theory," Treatise Geophys., **4**, pp. 73–91.

[114] Jiang, J., and Lapusta, N., 2016, "Deeper Penetration of Large Earthquakes on Seismically Quiescent Faults," Science, **352**(6291), pp. 1293–1297.

[115] Brune, J. N., Henyey, T. L., and Roy, R. F., 1969, "Heat Flow, Stress, and Rate of Slip Along the San Andreas Fault, California," J. Geophys. Res. Solid Earth, **74**(15), pp. 3821–3827.

[116] Heaton, T. H., 1990, "Evidence for and Implications of Self-Healing Pulses of Slip in Earthquake Rupture," Phys. Earth Planet. Inter., **64**(1), pp. 1–20.

[117] Zheng, G., and Rice, J. R., 1998, "Conditions Under Which Velocity-Weakening Friction Allows a Self-Healing Versus a Cracklike Mode of Rupture," Bull. Seismol. Soc. Am., **88**(6), pp. 1466–1483.

[118] Ben-Zion, Y., 2001, "Dynamic Ruptures in Recent Models of Earthquake Faults," J. Mech. Phys. Solids, **49**(9), pp. 2209–2244.

[119] Kanamori, H., and Rivera, L., 2006, *Earthquakes: Radiated Energy and the Physics of Faulting*, American Geophysical Union, Washington, DC, pp. 3–13.

[120] Shi, Z., Ben-Zion, Y., and Needleman, A., 2008, "Properties of Dynamic Rupture and Energy Partition in a Solid With a Frictional Interface," J. Mech. Phys. Solids, **56**(1), pp. 5–24.

[121] Noda, H., Dunham, E. M., and Rice, J. R., 2009, "Earthquake Ruptures With Thermal Weakening and the Operation of Major Faults at Low Overall Stress Levels," J. Geophys. Res. Solid Earth, **114**(B7).

[122] Noda, H., and Lapusta, N., 2013, "Stable Creeping Fault Segments can Become Destructive as a Result of Dynamic Weakening," Nature, **493**(7433), pp. 518–521.

[123] Dieterich, J. H., 2007, *Treatise on Geophysics*, 2nd ed., Elsevier, Oxford, pp. 93–110.

[124] Dieterich, J. H., 1979, "Modeling of Rock Friction: 1. Experimental Results and Constitutive Equations," J. Geophys. Res. Solid Earth, **84**(B5), pp. 2161–2168.

[125] Dieterich, J. H., 1981, *Constitutive Properties of Faults with Simulated Fault Gouge. In Mechanical Behavior of Crustal Rocks: The Handin*, Vol. 24, AGU, Washington, pp. 103–120.

[126] Ruina, A., 1983, "Slip Instability and State Variable Friction Laws," J. Geophys. Res. Solid Earth, **88**(B12), pp. 10359–10370.

[127] Blanpied, M., Lockner, D., and Byerlee, J., 1991, "Fault Stability Inferred From Granite Sliding Experiments at Hydrothermal Conditions," Geophys. Res. Lett., **18**(4), pp. 609–612.

[128] Blanpied, M. L., Lockner, D. A., and Byerlee, J. D., 1995, "Frictional Slip of Granite at Hydrothermal Conditions," J. Geophys. Res. Solid Earth, **100**(B7), pp. 13045–13064.

[129] Marone, C., 1998, "Laboratory-derived Friction Laws and Their Application to Seismic Faulting," Annu. Rev. Earth Planet. Sci., **26**(1), pp. 643–696.

[130] Kato, N., and Tullis, T. E., 2001, "A Composite Rate-and State-Dependent Law for Rock Friction," Geophys. Res. Lett., **28**(6), pp. 1103–1106.

[131] Kato, N., and Tullis, T. E., 2003, "Numerical Simulation of Seismic Cycles With a Composite Rate-and State-Dependent Friction law," Bull. Seismol. Soc. Am., **93**(2), pp. 841–853.

[132] Lu, X., 2009, "Combined Experimental and Numerical Study of Spontaneous Dynamic Rupture on Frictional Interfaces," Ph.D. thesis, Dissertation, California Institute of Technology, Pasadena, CA.

[133] Goldsby, D. L., and Tullis, T. E., 2011, "Flash Heating Leads to Low Frictional Strength of Crustal Rocks at Earthquake Slip Rates," Science, **334**(6053), pp. 216–218.

[134] Rice, J. R., 2006, "Heating and Weakening of Faults During Earthquake Slip," J. Geophys. Res. Solid Earth, **111**(B5), p. B05311.

[135] Beeler, N. M., Tullis, T. E., and Goldsby, D. L., 2008, "Constitutive Relationships and Physical Basis of Fault Strength Due to Flash Heating," J. Geophys. Res. Solid Earth, **113**(B1).

[136] Dieterich, J. H., and Kilgore, B. D., 1996, "Imaging Surface Contacts: Power Law Contact Distributions and Contact Stresses in Quartz, Calcite, Glass and Acrylic Plastic," Tectonophysics, **256**(1), pp. 219–239.

[137] Noda, H., Lapusta, N., and Rice, J. R., 2011, *Springer Series in Geomechanics and Geoengineering*, R. I. Borja, ed., Springer, Berlin, pp. 149–152.

[138] Thomas, M. Y., Lapusta, N., Noda, H., and Avouac, J.-P., 2014, "Quasi-Dynamic Versus Fully Dynamic Simulations of Earthquakes and Aseismic Slip With and Without Enhanced Coseismic Weakening," J. Geophys. Res. Solid Earth, **119**(3), pp. 1986–2004.

[139] Lapusta, N., Rice, J. R., Ben-Zion, Y., and Zheng, G., 2000, "Elastodynamic Analysis for Slow Tectonic Loading with Spontaneous Rupture Episodes on Faults with Rate-and State-Dependent Friction," J. Geophys. Res. Solid Earth, **105**(B10), pp. 23765–23789.

[140] Gori, M., Rubino, V., Rosakis, A., and Lapusta, N., 2019, "Nucleation, Slow Slip, and Dynamic Rupture Enabled by a Fluid-Injection Experimental Setup With Diagnostics Across Multiple Temporal Scales," manuscript in preparation.

[141] Abraham, F. F., Walkup, R., Gao, H., Duchaineau, M., De La Rubia, T. D., and Seager, M., 2002, "Simulating Materials Failure by Using up to one Billion Atoms and the World's Fastest Computer: Brittle Fracture," Proc. Natl. Acad. Sci. U. S. A., **99**(9), pp. 5777–5782.

[142] Buehler, M. J., Abraham, F. F., and Gao, H., 2003, "Hyperelasticity Governs Dynamic Fracture at a Critical Length Scale," Nature, **426**(6963), p. 141.

[143] Marder, M., 2006, "Supersonic Rupture of Rubber," J. Mech. Phys. Solids, **54**(3), pp. 491–532.

[144] Liepmann, H. W., and Roshko, A., 1957, *Elements of Gasdynamics*, Wiley, New York.

[145] Singh, R. P., and Parameswaran, V., 2003, "An Experimental Investigation of Dynamic Crack Propagation in a Brittle Material Reinforced with a Ductile Layer," Opt. Lasers Eng., **40**(4), pp. 289–306.

[146] Wu, H., Ma, G., and Xia, Y., 2004, "Experimental Study of Tensile Properties of PMMA at Intermediate Strain Rate," Mater. Lett., **58**(29), pp. 3681–3685.

[147] Richeton, J., Schlatter, G., Vecchio, K., Rémond, Y., and Ahzi, S., 2005, "A Unified Model for Stiffness Modulus of Amorphous Polymers Across Transition Temperatures and Strain Rates," Polymer, **46**(19), pp. 8194–8201.

[148] Mulliken, A., and Boyce, M., 2006, "Mechanics of the Rate-Dependent Elastic–Plastic Deformation of Glassy Polymers From Low to High Strain Rates," Int. J. Solids Struct., **43**(5), pp. 1331–1356.

[149] Fleck, N. A., Stronge, W., and Liu, J., 1990, "High Strain-Rate Shear Response of Polycarbonate and Polymethyl Methacrylate," Proc. R. Soc. London, Ser. A, **429**(1877), pp. 459–479.

[150] Schapery, R. A., 1965, "A Method of Viscoelastic Stress Analysis Using Elastic Solutions," J. Franklin Inst., **279**(4), pp. 268–289.

[151] Knauss, W., and Zhu, W., 2002, "Nonlinearly Viscoelastic Behavior of Polycarbonate. I. Response Under Pure Shear," Mech. Time-Depend. Mater., **6**(3), pp. 231–269.

[152] Rosakis, A. J., and Ravi-Chandar, K., 1986, "On Crack-Tip Stress State: an Experimental Evaluation of Three-Dimensional Effects," Int. J. Solids Struct., **22**(2), pp. 121–134.

[153] Rubino, V., Rosakis, A., and Lapusta, N., 2019, "Spatiotemporal Properties of Sub-Rayleigh and Supershear Ruptures Inferred From Full-Field Dynamic Imaging of Laboratory Experiments," J. Geophys. Res.